Geosci. Model Dev. Discuss., https://doi.org/10.5194/gmd-2019-84
Manuscript under review for journal Geosci. Model Dev.
Discussion started: 6 May 2019

Geoscientific Model Development Discussions

Improved methodologies for Earth system modelling of atmospheric soluble iron and observation comparisons using the Mechanism of Intermediate complexity for Modelling Iron (MIMI v.1.0).

Douglas S. Hamilton[1], Rachel A. Scanza[2], Yan Feng[3], Joe Guinness[4], Jasper F. Kok[5], Longlei Li[1], Xiaohong Liu[6], Sagar D. Rathod[7], Jessica S. Wan[1], Mingxuan Wu[6], and Natalie M. Mahowald[1]

1. Department of Earth and Atmospheric Science, Cornell University, Ithaca, NY, USA
2. Atmospheric Sciences and Global Change Division, Pacific Northwest National Laboratory, Richland, Washington, USA
3. Environmental Science Division, Argonne National Laboratory, Argonne, IL, USA
4. Department of Statistics and Data Science, Cornell University, Ithaca, NY, USA
5. Department of Atmospheric and Oceanic Sciences, University of California, Los Angeles, CA 90095, USA
6. Department of Atmospheric Science, University of Wyoming, Laramie, WY, USA
7. Department of Civil and Environmental Engineering, University of Illinois at Urbana-Champaign, Urbana, IL, USA

Abstract

Herein, we present the description of the Mechanism of Intermediate complexity for Modelling Iron (MIMI). This iron processing module was developed for use within Earth system models and has been updated within a modal aerosol framework from the original implementation in a bulk aerosol model. MIMI simulates the emission and atmospheric processing of two main sources of iron in aerosol prior to deposition: mineral dust and combustion processes. Atmospheric dissolution of insoluble to soluble iron is parametrized by an acidic interstitial reaction and a separate in-cloud reaction scheme based on observations of enhanced aerosol iron solubility in the presence of oxalate. Updates include a more comprehensive treatment of combustion iron emissions, improvements to the iron dissolution scheme, and an improved physical dust mobilization scheme. An extensive dataset consisting predominantly of cruise-based observations was compiled to compare to the model. The annual mean modelled concentration of surface-level total iron compared well with observations, but less so in the soluble fraction where observations are much more variable in space and time. Comparing model and observational data is sensitive to the definition of the average and the temporal and spatial range over which it is calculated. Through statistical analysis and examples, we show that a median or log-normal distribution is preferred when comparing with soluble iron observations. We redefined ocean deposition regions based on dominant iron emission sources and found that the daily variability in soluble iron simulated by MIMI was larger than that of previous model simulations. MIMI simulated a general increase in soluble iron deposition to Southern Hemisphere oceans by a factor of two to four compared with the previous version, which has implications for our understanding of the ocean biogeochemistry of these predominantly iron limited ocean regions.

Geosci. Model Dev. Discuss., https://doi.org/10.5194/gmd-2019-84
Manuscript under review for journal Geosci. Model Dev.
Discussion started: 6 May 2019

1 Introduction

Iron is an essential micronutrient for ocean primary productivity (Martin et al., 1991; Martin, 1990). Iron deficiency in oceans leads to high-nutrient low-chlorophyll (HNLC) conditions under which the photosynthetic productivity of phytoplankton is iron limited (Boyd et al., 2007; Jickells et al., 2005), and in other regions iron may be an important nutrient for nitrogen fixation by diazotrophs (Capone et al., 1997; Moore et al., 2013, 2006). Atmospheric deposition of bioavailable iron (i.e., the fraction of the total iron deposited that is readily available for ocean biota uptake) contained in aerosol is an important source of new iron for the remote open ocean (Duce and Tindale, 1991; Fung et al., 2000); therefore, iron impacts the ability of oceans to act as a sink of atmospheric carbon dioxide (Jickells et al., 2014; Moore et al., 2013).

Several definitions for bioavailable iron have been proposed. The solubility of iron is considered to be a key factor modulating its bioavailability (Baker et al., 2006a, 2006b); therefore, we consider bioavailable iron to be the dissolved (labile) iron in either a (II) or (III) oxidation state, and we define this as the soluble iron concentration throughout the manuscript. However, since most aerosol iron is insoluble at emission the processing of insoluble iron to a soluble form must occur during atmospheric transport. The acidic processing of iron contained in aerosol is one pathway under which soluble iron can be liberated from an insoluble form with decreasing pH (Duce and Tindale, 1991; Solmon et al., 2009; Zhu et al., 1997). Organic ligands, in particular oxalate, also increase iron solubility by weakening or cleaving the Fe–O bonds found in iron oxide minerals via complexation (Li et al., 2018; Panias et al., 1996), and in nature this reaction proceeds most rapidly in a slightly acidic aqueous medium, such as cloud droplets (Cornell and Schindler, 1987; Paris et al., 2011; Xu and Gao, 2008). Organic ligand processing has been estimated to increase soluble iron concentrations by up to 75% more than is achievable with acid processing alone (Ito, 2015; Johnson and Meskhidze, 2013; Myriokefalitakis et al., 2015; Scanza et al., 2018). However, there is no single mechanism that describes the observed inverse relationship of higher iron solubilities with decreasing iron concentrations (Sholkovitz et al., 2012). Rather, Mahowald et al. (2018) used a 1–D plume model to demonstrate that the observed trend can be explained by either the differences in iron solubility at emission or the atmospheric dissolution of insoluble iron. Thus, there is no observational constraint to indicate which is more likely, unless spatial distribution is also considered.

The recent increase in efforts to model iron solubility (Ito, 2015; Ito and Xu, 2014; Johnson and Meskhidze, 2013; Luo et al., 2008; Meskhidze et al., 2005; Myriokefalitakis et al., 2015; Scanza et al., 2018) reflects its importance for understanding biogeochemical cycles (Andreae and

Crutzen, 1997; Arimoto, 2001; Jickells et al., 2005; Mahowald, 2011) and how human activity may be perturbing them (Mahowald et al., 2009, 2017). However, the multi-faceted nature of how iron interacts within the Earth system results in many uncertainties regarding how best to represent the atmospheric iron cycle within models, which are themselves of varying complexity (Myriokefalitakis et al., 2018). To incorporate the processes currently thought to be the most significant (Journet et al., 2008; Meskhidze et al., 2005; Paris et al., 2011; Shi et al., 2012) and improve model-to-observation comparisons of the soluble iron fraction, particularly in remote ocean regions (Baker et al., 2006b; Ito, 2015; Mahowald et al., 2018; Matsui et al., 2018; Sholkovitz et al., 2012), model development has been focused on refining the atmospheric iron emission sources and subsequent atmospheric processing (Ito, 2015; Ito and Xu, 2014; Johnson and Meskhidze, 2013; Luo et al., 2008; Meskhidze et al., 2005; Myriokefalitakis et al., 2015; Scanza et al., 2018).

A recent multi-model evaluation of four global atmospheric iron cycle models (Myriokefalitakis et al., 2018) showed that total iron deposition is over-represented close to major dust source regions and under-represented in remote regions compared with observations from all four models. This is consistent with previous model intercomparisons studies that demonstrated the difficulty in simultaneously simulating both atmospheric concentrations and deposition fluxes of desert dust (Huneeus et al., 2011). Importantly, none of the atmospheric iron processing models can capture the high (>10%) solubilities measured over the Southern Ocean; this is potentially owing to the model processes associated with transport and aging of aerosol requiring further development (Ito et al. 2019, *in review*). Conclusions from Myriokefalitakis et al. suggest that future model improvements should focus on a more realistic aerosol size distribution and the representation of mineral-to-combustion sources of iron. Most of the development of the Mechanism of Intermediate Complexity for Modelling iron (MIMI), as described therein, focused on these points. First, we transitioned from a bulk aerosol scheme to a two-moment modal aerosol scheme (Liu et al., 2012), and second, we re-evaluated anthropogenic and fire combustion iron emissions. The modal aerosol scheme was used to calculate both aerosol size and number at each time-step within an updated global aerosol microphysics model, and the combustion emissions from Luo et al. (2008), which are likely to be underestimated (Matsui et al., 2018), were improved upon.

Ocean observations of iron, and its soluble fraction, are limited both spatially and temporally owing to the significant costs and logistical constraints associated with accumulating data from scientific cruises. Thus, there is an inherent disparity in attempting to compare climatological means calculated from temporally-chronological model results with observational means calculated from

temporally-limited and sporadic observations (e.g., Mahowald et al., 2008, 2009). This is important because natural aerosol emissions are variable on seasonal, annual, and decadal timescales, both in terms of primary natural iron emission sources (mineral dust and wildfires) and the source of aerosol acidity. For example, sulphuric acid from the oxidation of dimethyl sulphide and fire SO_2 (Bates et al., 1992; Chin and Jacob, 1996) have been observed to aid iron dissolution when far from anthropogenic acid sources (Zhuang et al., 1992). Limitations associated with the collection of continuous annual or inter-annual ship-based data across multiple remote ocean regions are immutable at present, which hinders the required derivation of basic statistical properties of such highly-variable data (Smith et al., 2017). Attention could therefore be given to the methodologies under which such model-observation comparisons are undertaken instead.

The present manuscript is presented in four parts. The first part (section 2) introduces updates made to the Bulk Aerosol Module (BAM) iron scheme of Scanza et al. (2018) and its implementation within the Modal Aerosol Module (MAM), with four modes (MAM4), within the Community Earth System Model (CESM). In the second part (section 3), we compare iron concentrations and the fractional solubility of iron with the observational data. Then the third part (section 4) compares our updated version of the model with its predecessor. Finally, we suggest further developments for atmospheric iron modelling and for comparing model results with sporadic observations (section 5).

2 Aerosol model

The present study improves upon the previous atmospheric iron cycle module developed for the Community Atmosphere Model (CAM) version 4 (CAM4) embedded in the CESM; we will refer to this version as BAM-Fe (Scanza et al., 2015, 2018) therein. We incorporated the iron module within the MAM framework (Liu et al., 2012, 2016) currently in the Department of Energy's Energy Exascale Earth System Model (E3SM; Golaz et al. (2019)) and the CAM versions 5 and 6 (CESM-CAM5/6; (Neale et al., 2010)); we refer to this new version of the iron model by its name (MIMI) throughout the manuscript. Table 1 serves as a refence and summarizes the modifications made for MIMI, which are discussed throughout the manuscript.

We use MAM4 with four simulated log-normal aerosol size modes: three modes (Aitken, accumulation, and coarse) containing iron and a fourth primary carbonaceous mode. Table 2

details the new combustion iron modal aerosol properties, while those of mineral dust iron follow existing dust aerosol properties (Liu et al., 2012). Generally, the modelled density of iron is similar to size-resolved ambient aerosol densities measured in Eastern China (Hu et al., 2012), which has significant dust and combustion aerosol sources. MIMI was initially implemented and tested within a development branch of CAM 5.3, as per Wu et al. (2017) and Wu et al. (2018), using Cheyenne (Computational and Information Systems Laboratory, 2017) and closely resembles CESM version 1.2.2. We used a 2.5° x 1.9° horizonal (longitude by latitude) resolution and 56 vertical layers up to 2 hPa. Stratiform microphysics followed a two-moment cloud microphysics scheme (Gettelman et al., 2010; Morrison and Gettelman, 2008). The other major aerosol species black carbon (BC), organic carbon, sea salt and sulphate (SO_4) were also simulated but are not explicitly examined here because we focused on the iron aerosol modelling. Fire emissions were vertically distributed between six injection height ranges: 0–0.1, 0.1–0.5, 0.5–1.0, 1.0–2.0, 2.0–3.0, and 3.0–6.0 km, as per AeroCom recommendations (Dentener et al., 2006). Fire emissions were uniformly distributed in model levels between height limits. Unless otherwise stated, aerosol and pre-cursor gas mass emissions were from the Climate Model Intercomparison Program (CMIP5) inventory (Lamarque et al., 2010). Major gas-phase oxidants (O_3,OH, NO_3 and HO_2) were supplied offline and were also from Lamarque et al. (2010). Meteorology (*U*, *V*, and *T*) was nudged to Modern-Era Retrospective analysis for Research and Applications (MERRA) data for 2006-2011. Unless otherwise stated, the last five years were used for analysis.

Table 1. Short summary of major differences between BAM-Fe and MIMI.

BAM-Fe (CAM4) Externally mixed bulk aerosol tracers with 4 size bins (0.1-1.0, 1.0-2.5, 2.5-5.0, 5.0-10.0 μm)	**MIMI (CAM5)** Internally mixed 2-moment aerosol tracers with 3 aerosol iron modes (Aitken, accumulation, coarse)
Static soil erodibility from offline maps: DEAD (Zender et al., 2003) scheme	Time-varying soil erodibility calculated online: Kok et al. (2014a) scheme
8 dust minerals, 5 of which are iron bearing	No change
Static Luo et al. combustion iron emissions	Static Luo et al. combustion iron emissions x5
Static Luo et al. fire iron emissions	Time-varying Fe:BC fire iron emission ratio
Surface fire iron emissions	Vertically distributed fire iron emissions
Static aerosol pH across aerosol size	Aerosol pH size dependent
Assumed oxalate concentration based on primary organic carbon	Assumed oxalate concentration based on secondary organic carbon
In-cloud aerosol concentrations based on simulated cloud fraction	Separate in-cloud and interstitial aerosol tracers

159 The model used in this study performed well when compared to observations from a variety of
160 different environments, and produced aerosol concentrations that were close to those of the multi-
161 model mean of similarly complex aerosol models (Fanourgakis et al., 2019).

162

163 **Table 2.** Combustion iron aerosol size and number properties.

Mode	Number mode diameter, D_{gn} (μm)	Geometric standard deviation (σ)	Volume mean particle diameter, D_{emit} (μm)[1]	Density, ρ (kg/m^3)
Aitken	0.03[a]	1.8[a]	0.0504	1500[c]
Accumulation	0.08[a]	1.8[a]	0.134	1500[c]
Coarse	1.00[b]	2.0[b]	2.06	2600[c]

164 1. $D_{emit} = D_{gn} \times \exp(1.5 \times (\ln(\sigma))^2)$
165 a. Liu et al. (2012)
166 b. Dentener et al. (2006) and Liu et al. (2012)
167 c. Wang et al. (2015)
168
169

170 **2.1 Dust modelling**

171 Desert dust was modelled via the Dust Entrainment And Deposition model (DEAD; Zender et al.,
172 2003), which was previously updated to include the brittle fragmentation theory of vertical dust
173 flux (Kok, 2011) on mineral size fractions (Albani et al., 2014; Scanza et al., 2015). We further
174 improved the emissions of dust in MAM to follow a physically-based vertical flux theory (Kok et
175 al., 2014a), which has been shown to significantly improve dust emissions (Kok et al., 2014b).
176 Notice that this method allowed for the removal of the soil erodibility map approach previously
177 employed by the DEAD scheme (Table 1), and still provided more accurate simulations of regional
178 dust emissions and concentration (Kok et al., 2014b). Dust aerosol optical depth (AOD) was
179 calculated using mineralogy-based radiation interactions as described by Scanza et al. (2015).
180 Dust emissions were tuned such that a global annual mean dust AOD of ~0.03 was attained, as
181 recommended by Ridley et al. (2016) and matching values in Scanza et al. (2015) for a similar
182 model configuration.

Dust minerology in MIMI is designed to be comprised of eight separate transported tracers: illite, kaolinite, montmorillonite, hematite, quartz, calcite, feldspar and gypsum (Scanza et al., 2015). Mineral soil distributions were supplied offline (Claquin et al., 1999) with the emission of each dust mineral species further refined following the brittle fragmentation theory (Scanza et al., 2015).

2.2 Iron modelling

The simulated lifecycle of iron can be grouped into three main stages: (1) iron emission to atmosphere, (2) physical-chemical iron processing during transport and (3) final iron deposition and, thus, loss from the atmosphere. In the following sections, we describe the emissions and subsequent atmospheric dissolution of iron (stages 1 and 2), while the effects of this on the magnitude of oceanic soluble iron deposition (stage 3) in MIMI are examined and compared to BAM-Fe in section 4.

Iron optical properties are currently considered to reflect those of hematite because this mineral contains 97% of the iron mass fraction (see section 2.3.1).

2.3 Iron emissions

MIMI contains three major iron emission sources: mineral dust, fires (defined here as the sum of wildfires and human-mediated biomass burning) and anthropogenic combustion (defined here as the sum of industrial and domestic biofuel burning). In the BAM-Fe version of the model, fire and anthropogenic combustion emissions were combined into a single static monthly mean value. In MIMI, fire emissions of iron were updated to be distinct from other combustion iron sources and were parametrized to track the BC emissions from fires using an Fe:BC ratio. Fire BC emissions were simulated to be time varying on a monthly scale, resulting in a much more pronounced seasonality to fire emissions (e.g., Giglio et al., 2013) compared to BAM-Fe where seasonality was not imposed.

For all iron species in each mode, the aerosol number emissions ($Fe_{emit,num}$) were calculated from the mass emissions within the same mode ($Fe_{emit,mass}$) using the properties in Table 2 following Liu et al. (2012),

$$Fe_{emit,num} = \frac{Fe_{emit,mass}}{\left(\frac{\pi}{6}\right) \times \rho \times D_{emit}^{3}} \quad \text{Equation 1}$$

2.3.1 Iron emissions within mineral dust

Based on previous research by Journet et al. (2008) and Ito and Xu (2014), the iron fraction in each mineral species was prescribed at emission as follows: 57.5% in hematite, 11% in smectite, 4% in illite, 0.24% in kaolinite, 0.34% in feldspar, and 0% in the remaining three mineral species (Table 3); which has been shown to improve the accuracy of the modelled total iron fraction estimated from dust (Scanza et al., 2018; Zhang et al., 2015). The mass of each of the eight mineral dust species advected at each model time step was the residual mineral mass (i.e., after the removal of the iron mass), such that the sum of all eight minerals and the total iron from mineral dust equalled unity, and hence, the original total singular dust mass emitted from the land surface.

Iron emissions from all eight mineral dust species were then partitioned into the four advected mineral-dust-bearing iron tracers (Table 3); iron tracers were defined as being (in)soluble and by the speed of the atmospheric reaction rate acting on them: slow or medium (Scanza et al., 2018). Note that, slow-soluble iron is only produced by atmospheric processing within the model.

Table 3. Mass fraction of iron in each simulated iron bearing mineral and allocation to each mineral iron tracer at emission.

	Mineral dust mass percent allocated to each dust iron tracer at emission				
Mineral	Med-soluble	Med-insoluble	Slow-soluble	Slow-insoluble	Total
Hematite	0.0%	0.0%	0.0%	57.5%	57.5%
Smectite	0.55%	10.45%	0.0%	0.0%	11.0%
Illite	0.11%	3.89%	0.0%	0.0%	4.0%
Kaolinite	0.01%	0.0%	0.0%	0.23%	0.24%
Feldspar	0.01%	0.0%	0.0%	0.33%	0.34%

2.3.2 Iron emissions from fires

Following Luo et al. (2008), we used observed Fe:BC mass ratios to estimate fine and coarse mode iron emissions from fires. An additional difference between BAM (CAM4) and MAM (CAM5) models is the emission dataset used to estimate global fire emissions of aerosol and trace gases. The BAM model uses adjusted AeroCom fire emissions (Dentener et al., 2006; Scanza et al.,

2018), while MAM uses CMIP5 fire emissions (Lamarque et al., 2010). Base fire BC emissions within the CMIP5 database are 2.55 Tg a^{-1} BC; however, the scaling of emissions from fires has been shown to be necessary to improve model to observed (aerosol optical depth and particulate matter) BC ratios (Reddington et al., 2016; Ward et al., 2012). Therefore, we globally scaled the fire iron emissions by a uniform factor of two, which is comparable with the overall lower scaling factor from a review of the literature by Reddington et al. (2016: Table 2). Fine mode iron emissions from fires were then segregated to assign 10% of the fine mode mass to the Aitken mode, with the remaining 90% assigned to the accumulation mode.

Table 4. Measured iron (Fe) and black carbon (BC) values (various units; as only the Fe:BC ratio is required they are not included) and the Fe/BC ratio. Calculated with three decimal places, ratio reported to one significant figure to reflect high uncertainty.

Biome	Reference	Fe	BC	Fe/BC
Cerrado	Yamasoe et al. (2000)	0.08	12.6	0.006
	Yamasoe et al. (2000)	0.05	6.5	0.008
	Ward et al. (1991)	0.9	3.3	0.273
	Mean Fe/BC ratio = 0.1			
Temperate	Ward et al. (1991)	0.1	5.0	0.020
	Mean Fe/BC ratio = 0.02			
Tropical	Luo et al. (2008)	-	-	0.020
	Artaxo et al. (2013)	179	2801	0.639
	Artaxo et al. (2013)	27	405	0.067
	Artaxo et al. (2013)	20	98	0.204
	Artaxo et al. (2013)	12	235	0.051
	Ward et al. (1991)	0.9	10	0.090
	Yamasoe et al. (2000)	0.03	7.3	0.004
	Yamasoe et al. (2000)	0.05	3.9	0.013
	Mean Fe/BC ratio = 0.06			
Global	Mean Fe/BC ratio = 0.06			

Luo et al. (2008) used a single Amazonian observational dataset in their study to determine the flux of iron from fires (Fe:BC). We extended this to incorporate other Amazonian fire (Fe:BC) data

and, importantly, non-Amazonian biome fire (Fe:BC) data, which are likely to have different combustion properties, and hence iron emissions (e.g., Akagi et al., 2011). From Table 4, we suggest that after adding 11 more data inventory values, Luo et al. likely under-represented the global fine mode Fe:BC ratio at 0.02. We instead used the global mean Fe:BC ratio from the additional data of 0.06. Conversely, Luo et al. likely over-represented the coarse mode Fe/BC ratio at 1.4. By including additional observational information from Artaxo et al. (2013) we reduced this to 1.0. Using size-segregated wet season (i.e., representing a locally-transported emission source) observation data from Artaxo et al. (2013), we estimated that the amount of BC mass in the coarse mode was 37% of fine mode mass. Overall this doubles the fractional contribution of fine mode (BAM: 0.1–1μm size bin, MAM: sum of Aitken and accumulation modes) iron emissions from fires (BAM-Fe: fine = 7% of total mass, MIMI: fine = 14% of total mass).

Using the soluble Fe:BC ratio of 0.02 reported in Luo et al. (2008) resulted in 33% solubility of fine mode iron from fires at emission, which is lower than the 46% reported in Oakes et al. (2012) and higher than the 12% reported in Ito (2013). As few data exist in the literature pertaining to coarse mode BC, or more importantly its ratio to iron, we retained the 4% solubility of iron in the coarse mode at emission, as suggested by Luo et al.

Total iron emissions from fires in MIMI were 2.2 Tg a^{-1} Fe (Aitken: 0.02 Tg a^{-1}, accumulation: 0.28 Tg a^{-1}, coarse: 1.9 Tg a^{-1}), representing an approximate increase in iron emissions from fires of around 25% compared with those from BAM-Fe, with most of the mass (86%) still in the coarse mode. Aerosol number concentrations were then calculated using the physical properties listed in Table 2. We adopted the methodology of Wang et al. (2015) by assuming that the density of iron aerosol from fires (and anthropogenic combustion) in the Aitken and accumulation modes matches that of BC, while in coarse mode matches mineral dust. The vertical distribution of iron emissions from fires were also updated in MIMI (BAM-Fe emitted all iron from fires at the surface) to account for pyro-convection, which lofts aerosol to higher altitudes at the point of emission within the model (Rémy et al., 2017; Sofiev et al., 2012; Wagner et al., 2018).

2.3.3 Iron emissions from anthropogenic combustion sources

Separate lines of evidence (Matsui et al., 2018, Ito et al. 2019 *in review*, Conway et al. 2019 *in review*) have shown that anthropogenic industrial iron emissions are highly likely to be larger than previously estimated (e.g., Ito, 2015; Luo et al., 2008; Myriokefalitakis et al., 2018a). Therefore, anthropogenic combustion emissions of iron in MIMI were the same as those in BAM-Fe, as first

reported by Luo et al. (2008), uniformly multiplied by a factor of five to bring into closer agreement with observations of industrial magnetite emissions in line with Matsui et al. (2018). Similar to fire emissions, 10% of fine size emissions were partitioned into the Aiken mode at emission, while the remainder was emitted into the accumulation mode. We retain the Luo et al. (2008) estimate of 4% combustion iron solubility at emission (Chuang et al., 2005). Calculations of aerosol number concentrations of combustion iron followed the same procedure as described for fire emissions in the previous section 2.3.2.

2.4 Atmospheric iron processing

Once airborne, iron undergoes a series of physical and chemical processing steps within the atmosphere, each working to alter the soluble iron fraction (i.e., its solubility). The MIMI atmospheric iron dissolution scheme is summarized in Table 5, with a full description reported previously by Scanza et al. (2018). Within each of the three iron-bearing aerosol size modes, six tracers of iron were advected within the model: medium-insoluble and medium-soluble mineral dust iron (containing both readily-released and medium-reactive mineral dust iron (Scanza et al., 2018)), slow-insoluble and slow-soluble mineral dust iron, and insoluble and soluble combustion iron (assumed to be medium reactive (Scanza et al., 2018)). Both proton and organic ligand promoted iron dissolution mechanisms were modelled. The proton promoted dissolution scheme was dependent upon an estimated $[H^+]$ and the simulated temperature. Organic ligand dissolution was dependent upon the simulated organic carbon concentration as oxalate (the main reactant) itself was not modelled. A structural model improvement was that MAM (CAM5) advected separate tracers for interstitial and cloud-borne aerosol, and so the proton and organic ligand promoted dissolution reactions were applied to each tracer, respectively.

Dust aerosol moving through areas containing acidic gases, with a pH 1–2, increases the solubility of the iron contained within it (Ingall et al., 2018; Longo et al., 2016; Meskhidze et al., 2003; Solmon et al., 2009); with minerology being a key factor determining the rate of dissolution at a given pH (Journet et al., 2008; Scanza et al., 2018). Modelled aerosol pH in MIMI was parametrised to depend only on the ratio of the calcium to sulphate aerosol concentration (Scanza et al., 2018). At each time step, if $[SO_4]$ > [Calcite], then the aerosol was assumed to be acidic with a low pH, while if $[SO_4]$ < [Calcite], then aerosol was assumed to be well buffered (Böke et al., 1999) and the pH = 7.5. In MIMI, we updated the pH calculation from BAM-Fe two-fold: (1) In BAM-Fe, pH was calculated as the mean across all four size bins (0.1–10 μm), while in MIMI, pH was calculated separately for each interstitial aerosol size mode. (2) Aerosol measurements of

316 pH have shown that interstitial aerosol is likely to be more acidic than was assumed in BAM-Fe
317 (Longo et al., 2016; Weber et al., 2016), even when taking into account declining sulphate levels
318 (Weber et al., 2016); therefore, we have lowered pH to 1 (from 2) in both the Aitken and
319 accumulation modes where sulphate aerosol dominates. However, in the coarse mode, where
320 dust dominates, we retained the lower pH boundary of 2. Furthermore, MAM aerosol was
321 simulated as an internally mixed aerosol; therefore, the SO_4:Ca ratio included the mixing of these
322 aerosol components within each mode.

323 The in-cloud organic dissolution reaction only occurs where cloud-borne aerosol are present. An
324 assumed oxalate concentration in MIMI was estimated based on the modelled organic carbon
325 concentration and could not exceed a maximum concentration threshold of 15 μmol/L (Scanza et
326 al., 2018). In BAM-Fe, oxalate was derived from the sum of both the primary and secondary
327 organic carbon aerosol concentrations, while in MIMI this was updated to be dependent only upon
328 the secondary organic carbon source because oxalate is itself a product of the oxidation of volatile
329 organic carbon gases (Myriokefalitakis et al., 2011). An additional term was added to the reaction
330 mechanism to account for the small amount of organic ligand processing proceeding by species
331 other than oxalate (Scanza et al., 2018).

332

333 **2.5 Observation and model iron calculations**

334 **2.5.1 Spatially aggregating limited observations**

335 The observations of total iron concentrations and the fractional solubility of iron used in this study
336 are the joint totals (1524 records) of those reported in Mahowald et al. (2009) and Myriokefalitakis
337 et al. (2018). However, many of these observations represent averages of only one or a few days
338 of iron and soluble iron measurements, and thus can be difficult to compare against annual, or
339 longer, mean time periods calculated within the model. Furthermore, building empirical
340 distributions of iron properties from observations requires a larger sample size than currently
341 available in many regions. We therefore tested how aggregating the observations spatially,
342 sometimes termed 'super-obbing', altered our model evaluation. Our objective was to capture the
343 small regional scale properties of iron, and not those at a point source; therefore, we assume that
344 the benefits gained by aggregating in this way, to help produce a statically useful amount of
345 observations, outweighs any potential biases.

346

Geosci. Model Dev. Discuss., https://doi.org/10.5194/gmd-2019-84
Manuscript under review for journal Geosci. Model Dev.
Discussion started: 6 May 2019

Geoscientific Model Development Discussions

Table 5. Summary of atmospheric processing reaction equations from Scanza et al. (2018). Here *l* represents either medium or slow reacting iron aerosol (combustion iron is modelled as medium). The pH calculation is updated to be calculated within each mode and oxalate ($C_2O_4^{2-}$) concentrations are calculated based only on the secondary organic aerosol (SOA) concentrations.

	Reaction equation	Reaction rate constituents
Acid processing of interstitial aerosol	Equation 2: $\frac{d}{dt}[Fe_{soluble}] = RFe_{i,acid} \times [Fe_{insoluble}]$ Equation 3: $\frac{d}{dt}[Fe_{insoluble}] = -\left(\frac{d}{dt}[Fe_{soluble}]\right)$	$RFe_{l,acid} = K_l(T) \times a(H^+)^{m_l} \times f(\nabla G_r) \times A_l \times MW_l$ $K_l(T)$ *is the temperature dependent rate coefficient (moles m^{-2} s^{-1})* $a(H^+)$ *is the proton concentration, with an empirical reaction order* m_l *If [SO_4] > [Calcite] then pH = 1 in Aitken and accumulation modes or 2 in coarse. Else pH = 7.5.* $f(\nabla G_r)$ *accounts for dissolution rate change with variation from equilibrium (equals 1 for simplicity (Luo et al., 2008))* A_l *is the specific surface area (m^2 g^{-1})* MW_l *is the molecular weight (g mol^{-1})*
Organic ligand processing of in-cloud aerosol	Equation 4: $\frac{d}{dt}[Fe_{soluble}] = RFe_{i,oxal} \times [Fe_{insoluble}]$ Equation 5: $\frac{d}{dt}[Fe_{insoluble}] = -\left(\frac{d}{dt}[Fe_{soluble}]\right)$	$RFe_{l,oxal} = a_l \times [C_2O_4^{2-}] + b_l$ *If l = medium (or combustion) iron:* *a = 2.3x10^{-7} μM^{-1} s^{-1}* *b = 4.8x10^{-7} s^{-1}* *If l = slow iron:* *a = 9.5x10^{-9} μM^{-1} s^{-1}* *b = 3.0x10^{-8} s^{-1}* *For longitude(i), latitude(j) and level(k):* $[C_2O_4^{2-}]_{i,j,k} = 150 \times \frac{[SOA_{i,j,k}]}{max[SOA]}$

Geosci. Model Dev. Discuss., https://doi.org/10.5194/gmd-2019-84
Manuscript under review for journal Geosci. Model Dev.
Discussion started: 6 May 2019

2.5.2 Variations in model temporal averaging

The model was run at a 30-minute time resolution. At each 30-minute timestep, soluble iron, total iron, and the ratio of soluble to total iron (iron solubility) were computed. The model output was S_i, (daily mean soluble iron concentration on day i), T_i (daily mean total iron concentration on day i), and R_i (daily mean iron solubility on day i). Note that R_i is the daily mean of the calculated 30-minute solubilities and hence is not equal to S_i / T_i. We define online solubility as the average-of-ratios and was calculated as follows:

$$(\sum_{i=1}^{n} R_i)/n \qquad \text{Equation 6}$$

where n represents the total number of records over which the average was calculated. Online solubility is reported throughout this study. In section 5.2, we then compare the average-of-ratios to the ratio-of-averages (defined as offline solubility), calculated as follows:

$$\frac{(\sum_{i=1}^{n} S_i)\ /n}{(\sum_{i=1}^{n} T_i)\ /n} = \frac{\bar{S}}{\bar{T}} \qquad \text{Equation 7}$$

where $\bar{S}$ and $\bar{T}$ are the grid cell averages of soluble and total iron concentrations, respectively, over the total time period considered in this study (2007 to 2011). While equation 7 is common within the literature, this methodology can produce larger variability in iron solubility across grid cells because it is based on both soluble and total iron annual mean concentration. In the online method, variability is reduced as extreme values in soluble and total iron concentrations generally do not occur at the same time. We can define the occurrence of extreme values, with respect to the time frame considered, by analysing a relative Z-score metric, calculated as follows:

$$Z_{Fe,t} = \frac{(Fe_t - \overline{Fe_t})}{\sigma Fe_t} \quad or \quad Z_{Fe,s} = \frac{(Fe_s - \overline{Fe_s})}{\sigma Fe_s} \qquad \text{Equation 8}$$

where Fe is either total (Fe_t) or soluble (Fe_s) iron. The relative normalized Z-score can then be calculated as follows:

$$\sum_{i=1}^{n} (z_{t,i} - z_{s,i}) / z_{t,i} \qquad \text{Equation 9}$$

where $Z_{t,i}$ and $Z_{s,i}$ are the Z-scores of total and soluble iron concentrations, respectively, at each grid cell for each time step *i*. The Z-score metric provides a relative direction and distance of an instantaneous value with respect to its mean. The Z-score is reported in multiples of the standard deviation (Equation 8); therefore, a Z-score of zero indicates that the data point value is identical to the mean. To assess the relative difference in the variability, at a given time, between the modelled total and soluble iron concentration and its mean we calculated the difference in Z-scores between total and soluble iron concentrations and normalized it using the Z-score of total iron concentration (Equation 9). Note that the Z-score of the soluble iron concentration could also be used to normalise the difference. This method allows for the examination of how the occurrence of extreme concentration values in total and soluble iron influences the method of solubility calculation (Equation 6 vs. Equation 7).

2.6 Iron ocean deposition source apportionment

An ocean deposition source apportionment sub-study was designed to classify ocean deposition regions according to the dominant atmospheric soluble iron sources, rather than ocean basins defined from a more traditional physical oceanographic viewpoint (e.g., Gregg et al., 2003). By incorporating recent model estimates for dust and the importance of combustion iron emissions (Luo et al., 2008; Matsui et al., 2018) the seven large-scale source regions defined in Mahowald et al. (2008) were modified slightly to separate the major dust iron source regions from combustion iron source regions. This resulted in a total of 10 iron emission source regions (Fig. 1; see also Table S1 for details).

Simulations in the source apportionment study used BAM-Fe, as described in Scanza et al. (2018) with slight modification. Briefly, anthropogenic combustion emissions were increased by a uniform factor of five, and iron from fires followed the updated Fe:BC ratio (Table 4) and seasonal variability in the fire BC emissions; all as per MIMI. Aerosols were externally mixed in BAM, and therefore altering the regional aerosol loading did not affect aerosol transport or deposition in the more significant way it could in MAM, in which aerosol are internally mixed. This information was then used in Section 4 to compare the differences in daily mean deposition of soluble iron between the BAM-Fe and MIMI models within each defined ocean region.

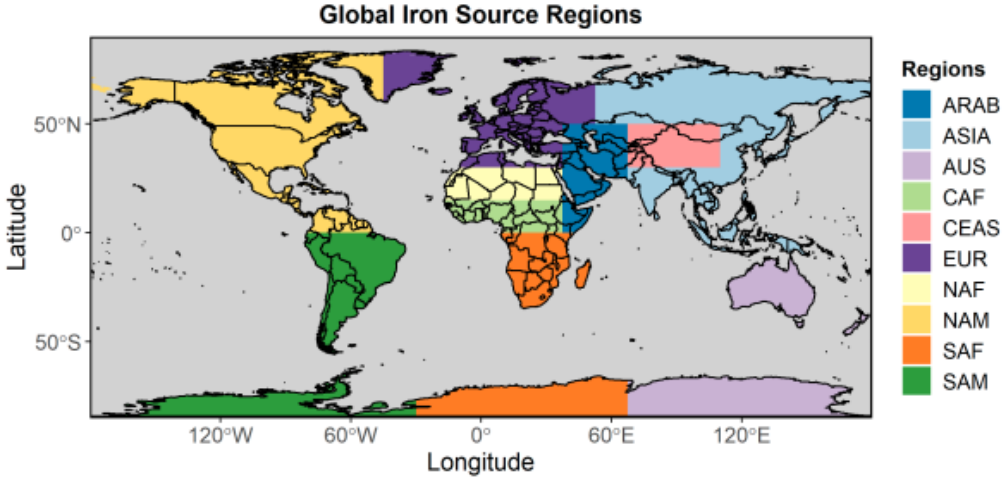

406

407 **Figure 1**. Major iron emission source regions.

408

409 **3 Modelled dust and iron concentrations compared to observations**

410 In terms of Earth system modelling, and the biogeochemistry that connects the land–atmosphere–
411 ocean components, we are ultimately motivated here to improve the magnitude of the atmosphere
412 to ocean iron deposition flux and its fractional solubility (from which the soluble iron flux can be
413 derived). We compare the model results with a series of observations, and herein, highlight some
414 of the problems discovered when directly comparing with a sporadic (in both space and time)
415 observation dataset, as is currently common practice (Myriokefalitakis et al., 2018)

416

417 **3.1 Global dust comparisons**

418 Comparison of dust AOD with regional dust AOD observations (Fig. 2) from the AERONET
419 observational datasets (Holben et al., 2000), as subsampled in Albani et al. (2014), shows good
420 agreement (correlation: $r^2 = 0.64$). This results in MAM annual global mean emissions of 3250 ±
421 77 Tg dust a^{-1}, which is at the higher end of literature estimates of ~500–4000 Tg dust a^{-1} (Bullard
422 et al., 2016; Huneeus et al., 2011; Kok et al., 2017). Dust emissions in MAM are 84 ± 4% higher
423 than our previous mean of 1768 Tg dust a^{-1} in BAM (Scanza et al., 2018), because dust lifetime
424 has proportionally decreased (Table S2). Both dust concentrations and deposition are simulated
425 well within MIMI, improving on previous dust modelling complications related to underestimating
426 dust deposition when tuned to dust concentration (Huneeus et al., 2011).

Geosci. Model Dev. Discuss., https://doi.org/10.5194/gmd-2019-84
Manuscript under review for journal Geosci. Model Dev.
Discussion started: 6 May 2019

427

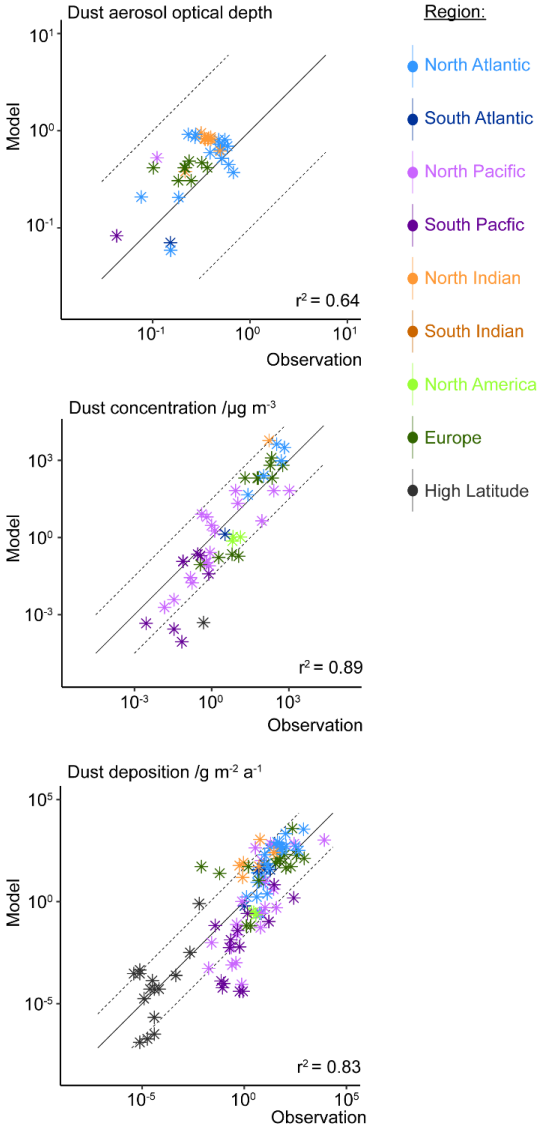

428

429

430 **Figure 2.** Dust aerosol optical depth, surface concentrations and deposition in modal aerosol
431 model and observations (Albani et al., 2014; Holben et al., 2000).

432

Geosci. Model Dev. Discuss., https://doi.org/10.5194/gmd-2019-84
Manuscript under review for journal Geosci. Model Dev.
Discussion started: 6 May 2019

433 **3.2 High latitude dust and iron aerosol**

434

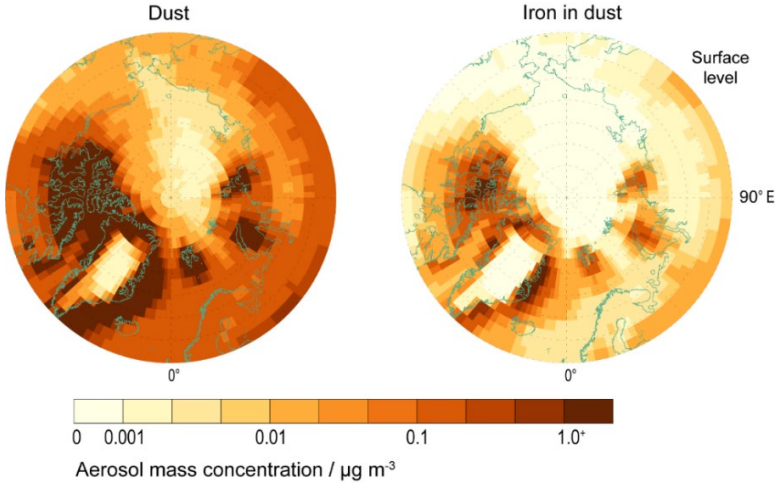

435

436

437 **Figure 3.** High latitude (>60ºN) dust (sum of eight mineral species and four dust-iron species)
438 and iron (sum of four dust-iron species) mass concentrations (μg m^{-3}) at the surface model level.

439

440 Including the parametrization of Kok et al. (2014a) removes the requirement of a soil erodibility
441 map (Table 1). In addition, in previous versions of the model, the high latitude dust sources were
442 zeroed, because there were no observations at that time for high latitude sources of dust (Albani
443 et al., 2014). However, more recent observations have suggested high latitude dust sources do
444 exist (Bullard et al., 2016; Crusius et al., 2011; Tobo et al., 2019), often related glacial processes
445 (Bullard, 2017) with a higher fraction of bioavailable iron relative to lower latitude dust sources
446 (Shoenfelt et al., 2017). Thus, for the new version of the model we have allowed for the inclusion
447 of high latitude dust sources (Fig. 3). In general, aerosol dust and iron concentrations peak closest
448 towards the coast lines and during summer. Emissions of dust from >50ºN are ~1.3 ± 0.2% of the
449 global dust total, which is half of the estimates derived from field and satellite data at 2–3% of the
450 global total (Bullard, 2017; Bullard et al., 2016). However, the resulting magnitude and seasonality
451 of dust concentrations has been shown in a recent study to be consistent with observed
452 measurements from Svalbard (Tobo et al., 2019).

453

Geosci. Model Dev. Discuss., https://doi.org/10.5194/gmd-2019-84
Manuscript under review for journal Geosci. Model Dev.
Discussion started: 6 May 2019

3.3 Global iron aerosol concentration and fractional solubility

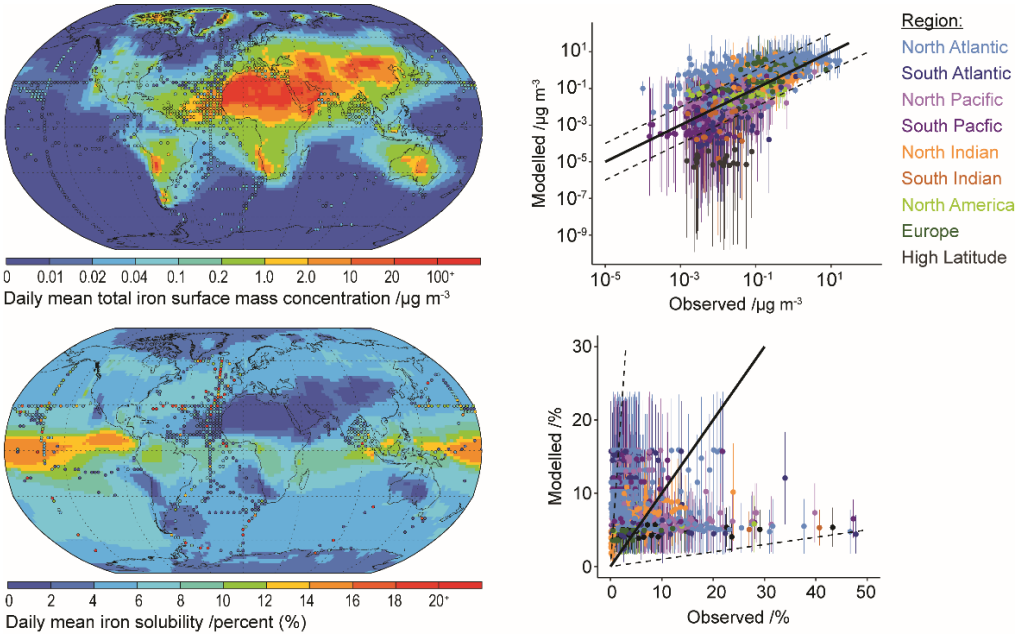

Figure 4. Daily mean model total iron concentration and solubility from 2007 to 2011. Observations (circles) overlaid (at resolution of the model grid) as a mean from 1524 individual records in Mahowald et al. (2009) and in Myriokefalitakis et al. (2018). Also shown are scatter plots of the model mean and standard deviation compared to each available observation and identified by oceanic region.

There are several propositions explaining the sources of soluble iron, and the inverse relationship between total iron amount and iron solubility (Sholkovitz et al., 2012). While total iron mass concentrations are dominated by desert dust sources, soluble iron can be a product of mineral dust processed in the atmosphere or emitted from different sources (e.g., Chuang et al., 2005; Guieu et al., 2005; Luo et al., 2008; Meskhidze et al., 2003; Schroth et al., 2009). Previous studies have shown that either of these can explain the inverse relationship, and that the spatial distribution of data is required to provide more information (Mahowald et al., 2018). Therefore, we explored how to best use the spatial data to compare with the model results. The five-year (2007

Geosci. Model Dev. Discuss., https://doi.org/10.5194/gmd-2019-84
Manuscript under review for journal Geosci. Model Dev.
Discussion started: 6 May 2019

472 to 2011) mean iron concentration from MIMI is compared to an extensive dataset of observations
473 of total iron and its fractional solubility (Fig. 4). Except for between 30 and 60ºN in the North
474 Pacific (and near Hawaii) and a latitudinal band ~30ºN in the North Atlantic, the model captures
475 the mean observational total iron concentration well.

476

477

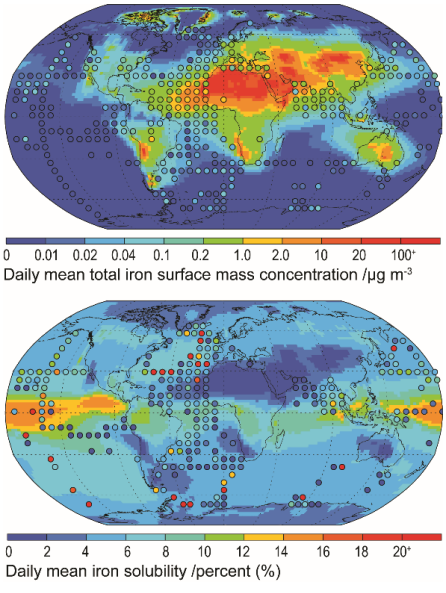

478

479

480 **Figure 5.** Daily mean model total iron concentration and solubility from 2007 to 2011.
481 Observations (circles) overlaid (at resolution one-third of the model grid) as a mean from 1524
482 individual records in Mahowald et al. (2009) and in Myriokefalitakis et al. (2018).

483

484 Aggregating observations onto a lower resolution grid (sometimes termed 'super-obbing')
485 compared with the model can help reduce the representation error when comparing with such
486 limited observations (Schutgens et al., 2017). Fig. 5 uses an observational resolution one-third
487 that of the model and the model-to-observation comparison of the mean state is thus improved.
488 Persistent observation-based features of the local environment become more obvious while,
489 conversely, less frequent ones diminish. At this observational resolution, the low total iron

490 concentrations in the North Atlantic ~30ºN, as seen in Fig. 4, are perhaps not a common feature,
491 and the model much more precisely represents the climatological state here than Fig. 4 might
492 suggest. However, examining the North Pacific reveals that the model imprecisely represents the
493 mean state here. Potential missing iron sources in remote regions, such as the North Pacific,
494 include: (1) shipping emissions (Ito, 2013), which have a high iron content from oil combustion
495 (Schroth et al., 2009); (2) volcanic emissions, which provide a localized "fertilizer" to the surface
496 ocean owing to the macronutrients and trace metal nutrients contained within them (Achterberg
497 et al., 2013; Langmann et al., 2010; Rogan et al., 2016); and (3) low Asian and South American
498 aerosol concentrations, either through underrepresenting combustion emission sources (Matsui
499 et al., 2018) or in the transport and deposition of aerosol within these regions (Wu et al., 2018).
500 These are discussed in more detail in the discussion sections 5.1 and 5.2.

501

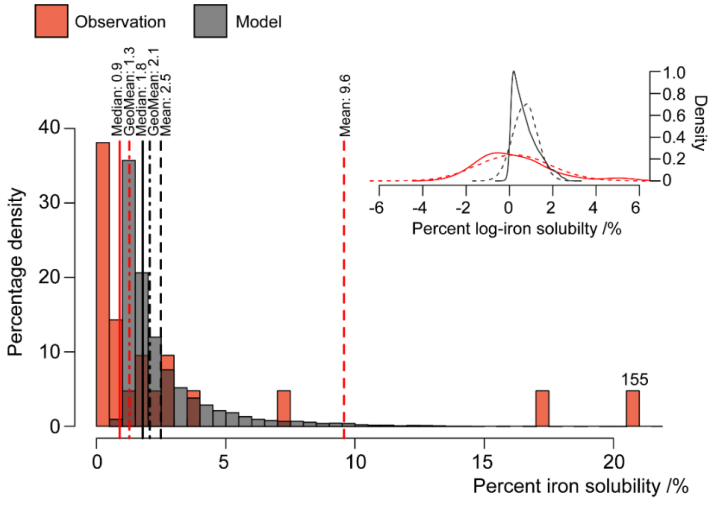

502

503

504 **Figure 6.** Histogram of observations (n = 21) and daily model results (2007 to 2011) of iron
505 solubility between 16 to 20ºN and 27 to 32ºW (one observation point and nine co-located model
506 grid cells in Fig. 4). Mean (dashed lines), geometric mean (dot-dash lines) and median (full line)
507 values shown above respective dataset colour line. Note that the single observation value of
508 155% is off the scale and placed as such with value given above. **Insert.** Log-plot for the same
509 data (solid lines) with projected log-normal distribution from mean and standard deviation of data
510 (dashed lines).

Geosci. Model Dev. Discuss., https://doi.org/10.5194/gmd-2019-84
Manuscript under review for journal Geosci. Model Dev.
Discussion started: 6 May 2019

511

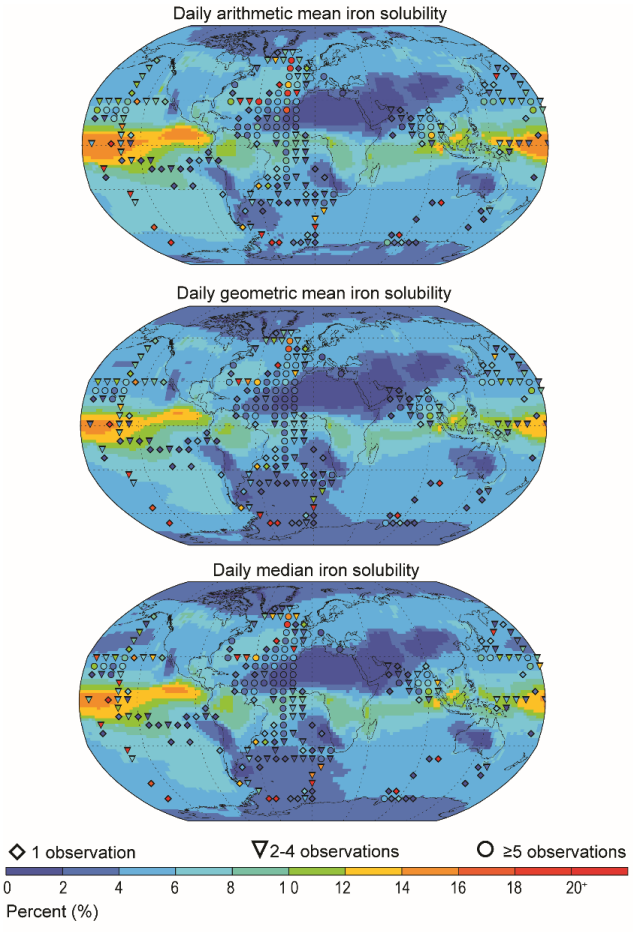

512

513 **Figure 7.** Daily arithmetic mean, geometric mean, and median model solubility (2007 to 2011).
514 Observations overlaid (at resolution one-third of the model grid) as either the arithmetic mean,
515 geometric mean or median, respective to the model averaging. Number of observations denoted
516 by symbol: lowest confidence (one observation, diamond); intermediate confidence (two to four
517 observations, triangle); highest confidence (≥five observations, circle).

518

519 In terms of iron solubility (soluble iron concentration / total iron concentration), the model is not
520 capturing the observational mean state in many regions (Fig. 5). A detailed examination of the
521 observation point at 18ºN and 330ºE (anomalous green point surrounded by blue points in the
522 North African outflow plume in Fig. 4) and the nine model grid cells co-located with it in Fig. 6

shows how a single high observation (155% percent solubility) is causing a representation issue (see also section 4.3.1 regarding soluble iron deposition). Both model and observation histogram distributions are similar, as are the median and geometric mean values. However, the arithmetic means are not similar and while a high observation value of 155% is likely to be an outlier, and should be at most 100%, it still informs us about what is possible and simply discounting it (even at an adjusted 100%) would require strong justification. It is therefore advisable to instead alter the estimator of the average. Comparing model to observation differences calculated using the median or geometric mean reveals that they are similar in magnitude, as one would expect for log-normally distributed data (Fig. 6 insert). Although the median is robust with respect to outliers, the model results may not exhibit a uniform Gaussian distribution (Fig. 6 insert; solid compared to dashed lines) and often the amount of available observations is also low (Fig. 7) suggesting that its use also requires careful consideration. An equivalent methodology to the geometric mean in Fig. 7 would be to first log transform the data before calculating the arithmetic mean. Arguments pertaining to the appropriate methodology for comparing model results to temporally limited observations extend beyond the iron aerosol examination in this study to all aerosol comparisons with limited observations.

3.4 Calculating iron solubility

It is interesting to note the effect that the order of operations (taking the average-of-ratios compared to the ratio-of-averages) has when calculating iron solubility (Fig. 8). Throughout the manuscript, percent iron solubility was calculated at each model time step (30 minutes) and then the daily mean output analysed (online; Equation 6) at an annual or 5 year mean time resolution. It is also acceptable to use the simulated soluble and total iron concentrations to generate the annual or 5 year mean iron solubility in a postprocessing step (offline; Equation 7). The resulting differences between methods is not insignificant however, with the offline method creating a distribution in which, low iron solubility is generally lower and the highest (>18%) iron solubilities are generally higher.

Geosci. Model Dev. Discuss., https://doi.org/10.5194/gmd-2019-84
Manuscript under review for journal Geosci. Model Dev.
Discussion started: 6 May 2019

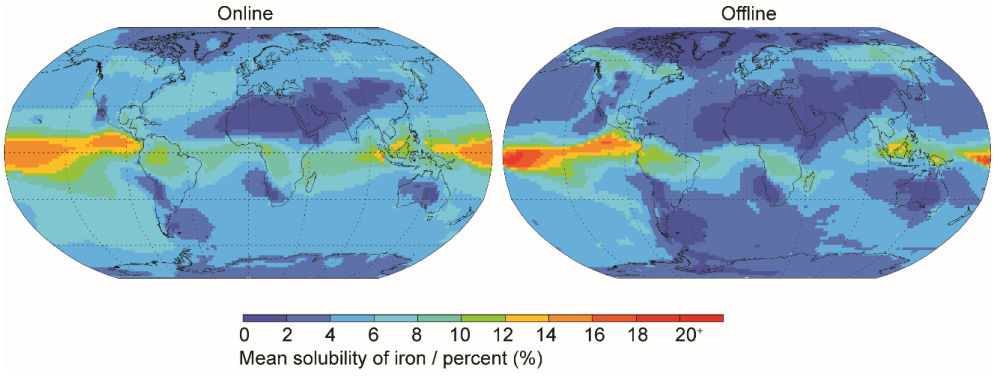

552

553 **Figure 8**. Mean solubility of iron when solubility is calculated at each 30 min model time step
554 ('online') and when it is calculated post processing from the daily mean soluble and total iron
555 concentration ('offline').

556

557 The average relative Z-score (Equations 8 and 9) is around zero for most model grid cells (Fig.
558 9) indicating that they mostly followed similar temporal and relative magnitude trends. However,
559 even if the average relative Z-scores are around zero and the ratio of relative standard deviations
560 is around one, the ratio of online:offline calculated iron solubility is most likely >1. Temporal
561 differences in the soluble and total iron concentration might therefore be controlling the overall
562 solubility at each grid cell. We also find that the ratio of online and offline solubility is >1 for most
563 of the cases when the ratio of relative standard deviations of soluble and total iron is <1 (Fig. S1),
564 indicating that the differences in the both methods of solubility calculation are sensitive to the
565 differences in relative size of the tails of the distribution. That is, if soluble iron has narrower tails
566 compared to total iron at any grid cell, it is highly likely that a higher solubility will be obtained in
567 the online method compared to the offline. We also find that the ratio of online and offline solubility
568 is >1 for most of the cases when the ratio of relative standard deviations of soluble and total iron
569 is <1 (Fig. S1), indicating that the differences in the both methods of solubility calculation are
570 sensitive to the differences in relative size of the tails of the distribution. That is, if soluble iron has
571 narrower tails compared to total iron at any grid cell, it is highly likely that a higher solubility will
572 be obtained in the online method compared to the offline. The ratio of the tails of soluble and total
573 iron are generally found around regions with highest temporal variability in emissions and
574 modelled solubilization of insoluble iron (Fig S1).

575

Geosci. Model Dev. Discuss., https://doi.org/10.5194/gmd-2019-84
Manuscript under review for journal Geosci. Model Dev.
Discussion started: 6 May 2019

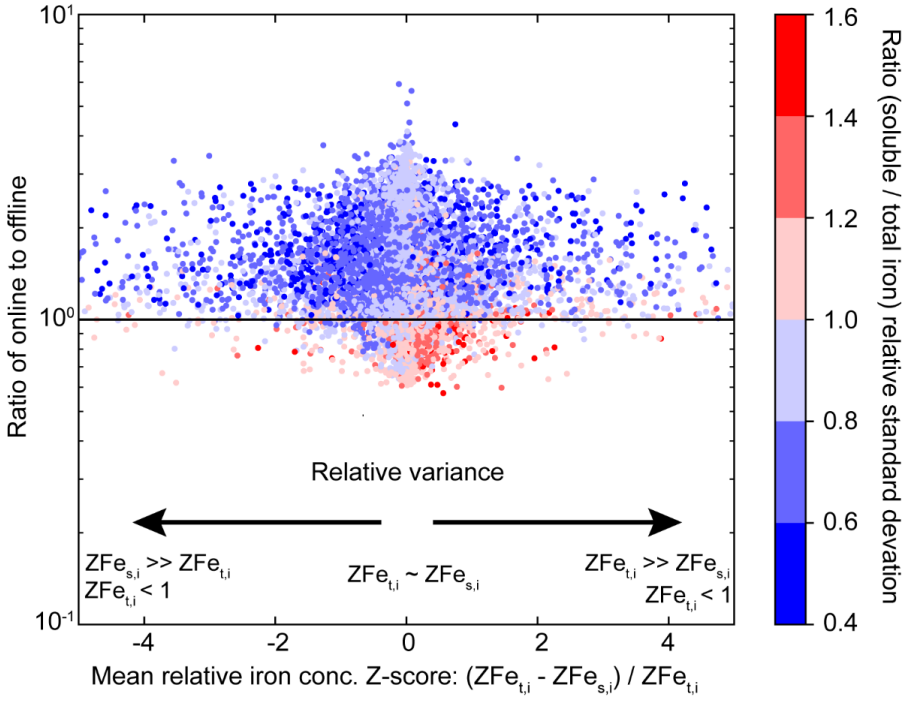

576

577 **Figure 9.** Relationship of online to offline derived iron solubility to the relative Z-score for total
578 (ZFe_t) and soluble (ZFe_s) iron and the relative standard deviation ($\sigma Fe / \overline{Fe}$) at each grid cell for
579 the year 2007.

580

581 Field measurements have generally suggested an inverse relationship between total and soluble
582 iron concentrations (Myriokefalitakis et al., 2018). This means that high total iron concentrations
583 are generally accompanied by low soluble iron concentrations and vice versa. By assuming that
584 the field measurements faithfully represented the actual average values of soluble and total iron
585 concentration at those locations, we implicitly assume that all the measurements have a Z-score
586 of zero. In Fig. 9 we show that this is not the case with the modelled results, and the two variables
587 can be relatively farther from their respective means even when averaged over the modelled time
588 period.

589 Sensitivity of a result to the order of operations extends beyond iron solubility to any variable that
590 is calculated in a similar manner, and current multi-model inter-comparison project (MIP) protocols

do not explicitly account for this. However, the effects of outliers, in both online and offline methods, can be reduced by employing the geometric mean and has been used in some MIP's (e.g., Mann et al., 2014). It will be also be important to consider differences in the solubility of iron induced by the choice of the order of operations as ocean biogeochemical models move away from using offline results from global climate models to online results within Earth system models, which are designed to couple the two components at each time step. For short term interactions between deposited iron and ocean biota shorter term averaging may be more important (e.g., Guieu et al., 2014), but for long term period accumulation of iron that is (re-)cycling in the oceans, the longer term average may be more appropriate (Moore et al., 2013). One should be aware, however, that iron is readily removed from the ocean mixed layer, and thus, the lifetime of iron may well be short enough for the 'online' calculation to be more appropriate much of the time (Guieu et al., 2014).

4.0 MIMI vs. BAM-Fe

In this section, we discuss how the new modal aerosol mode version of MIMI compares to its predecessor bulk aerosol model version (BAM-Fe) throughout all three stages of the atmospheric iron life-cycle.

4.1 Iron emission comparison

Globally averaged emissions of dust are ~80% higher and the iron it contains ~120% higher in MIMI compared to those in BAM-Fe (Table 6). Although both models are globally tuned to a similar dust AOD, and based within the same host model (CESM), changing from a bulk aerosol to a modal scheme (e.g., Albani et al., 2014; Scanza et al., 2015) reduces the aerosol lifetime significantly (Liu et al., 2012 and Table S2). The spatial distribution of dust emissions is also different following the move to the Kok et al. (2014a, 2014b) parameterization (Table 1), resulting in the spatial distribution of dust AOD also altering (Fig. S2). Total combustion iron emissions (sum of fires and anthropogenic combustion activity) in MIMI are also higher than previous estimates by a factor of between two and three (Table 6), reflecting the recently growing evidence indicating that they have been previously underestimated (Matsui et al., 2018, Ito et al. 2019 *in review*, Conway et al. 2019 *in review*).

Geosci. Model Dev. Discuss., https://doi.org/10.5194/gmd-2019-84
Manuscript under review for journal Geosci. Model Dev.
Discussion started: 6 May 2019

622 **Table 6.** Dust, fire, and combustion emissions of iron and relevant co-emitted aerosol emissions
623 (to two significant figures). Multi-model emission range from the four global atmospheric iron
624 models (including BAM-Fe) reported in Myriokefalitakis et al. (2018). Fine (sum of Aiken and
625 accumulation modes) and coarse (coarse mode) mass emissions also given for fire and
626 combustion iron.

627

	Annual mean emissions /Tg a^{-1}			
	BAM-Fe	MIMI	Luo et al. (2008)	Multi model
Dust	1800	3200	1600	1200–5100
Dust iron	57	126	55	38–134
Fire&Comb. iron	1.9	5.5	1.7	1.8–2.7
Fire BC	4.1	2.6	3.6	
Total fire iron	1.2	2.2	1.1	
Fine, Coarse	0.08, 1.1	0.30, 1.90	0.07, 1.00	
Combustion BC	4.6	5.0	5.0	
Total comb. iron	0.66	3.3	0.66	
Fine, Coarse	0.10, 0.56	0.50, 2.80	0.10, 0.56	

628

629

630 **4.2 Iron atmospheric processing comparison**

631 There is a much lower aerosol pH in the fine aerosol modes (Aiken and accumulation) in MIMI
632 compared to that in BAM-Fe (Fig. 10). This is due to a combination of resolving pH in each aerosol
633 size mode in MIMI and the subsequent lowering of the pH value (1) being applied in the two fine
634 aerosol modes (Aitken and accumulation). Conversely, dust dominating the coarse aerosol mode
635 provides more of an opportunity for [Calcite] > [SO_4] in this aerosol size fraction, resulting in most
636 continental areas having a high coarse mode aerosol pH in MIMI compared with the higher pH
637 being much more localized to the major desert regions in BAM-Fe. Acidic processing of iron in
638 MIMI is therefore faster globally in the two finer aerosol modes compared to the BAM-Fe fine
639 mode, but generally slower over continental regions in the coarse mode than in BAM-Fe.

640

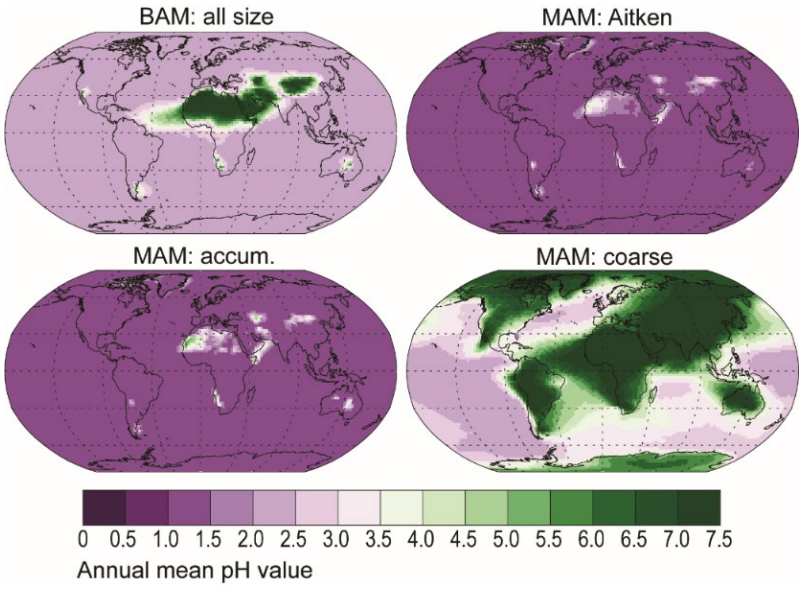

641

642 **Figure 10**. Surface level annual mean interstitial aerosol pH (see methods for pH calculation).

643

644 Model physics, and hence simulated cloud cover, is significantly different between CAM4 and
645 CAM5. Fig. 11 shows the relative model difference in the oxalate dissolution reaction between
646 MIMI, which also includes an increase in the tuning factor by an order of magnitude (from 15 to
647 150; Table 5), and BAM-Fe by normalising by the simulated cloud fraction in each model
648 respectively. The effect of oxalate on iron dissolution is larger in MIMI over extra-tropical ocean
649 regions, where iron models underrepresent solubility (Myriokefalitakis et al., 2018), and land
650 regions which are dense in tropical vegetation or industry (both centres of large aerosol pre-cursor
651 gas emissions).

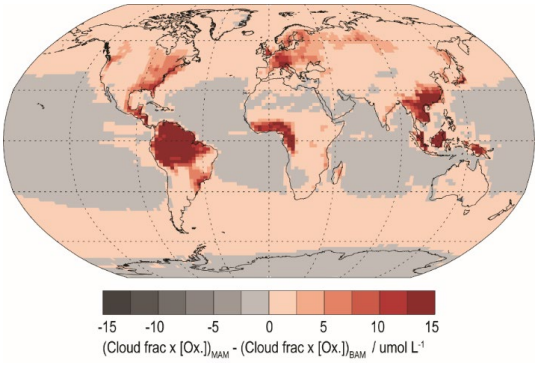

652

653

654 **Figure 11.** Relative difference in organic ligand reaction on in-cloud iron aerosol dissolution
655 between MIMI and BAM-Fe versions of MIMI. Due to significant differences in simulated cloud
656 cover between CAM4 and CAM5 oxalate concentrations [Ox.] are multiplied by the model
657 simulated cloud fraction in this figure.

658

659 **4.3 Iron ocean deposition flux comparison**

660 Similar to the previous study by Scanza et al. (2018), we report the amount of total and soluble
661 iron deposited in each of the major ocean basins (Table 7) as defined by Gregg et al. (2003). We
662 find that, in MIMI the amount of total iron deposited in all ocean basins is approximately double
663 that estimated in BAM-Fe, while soluble iron deposition is similar. The larger mineral dust flux in
664 MIMI is driving most of the increases to total iron deposition because it is the primary iron source
665 (Table 6). In general, the magnitude of soluble iron deposition to the oceans is more evenly
666 distributed across hemispheres in MIMI owing to a major reduction (approximately one half) in
667 the equatorial North Central Atlantic basin flux and increases to Southern Hemisphere (SH) ocean
668 fluxes of a factor of two to four. There are significant increases in combustion iron deposition in
669 all equatorial and Northern Hemisphere (NH) ocean basins, driven by the 5-fold increase in
670 combustion emissions implemented in MIMI.

671

672

673

674

Geosci. Model Dev. Discuss., https://doi.org/10.5194/gmd-2019-84
Manuscript under review for journal Geosci. Model Dev.
Discussion started: 6 May 2019

Geoscientific Model Development Discussions

675 **Table 7.** Global and regional ocean basin deposition (Gg a^{-1}) of total and soluble iron in BAM-Fe
676 (Scanza et al., 2018) and MIMI (this study). Deposition was multiplied by the ocean fraction of
677 model grid cell and is reported at two significant figures. Percent contribution from combustion
678 iron to deposition also given. Ocean basins are those defined by Gregg et al. (2003) and
679 previously used by Scanza et al. (2018).

680

	Dust and comb. deposition /Gg a^{-1}				Percent from combustion /%			
	Total iron		Soluble iron		Total iron		Soluble iron	
	BAM-Fe	MIMI	BAM-Fe	MIMI	BAM-Fe	MIMI	BAM-Fe	MIMI
Global	**12000**	**26000**	**500**	**530**	**3.3**	**5.0**	**7.6**	**23**
N. Atlantic	1800	5300	46	86	1.9	2.9	4.8	11
N. Pacific	730	1200	35	36	10	19	15	43
NC. Atlantic	2900	5700	92	89	0.30	0.52	0.9	3.7
NC. Pacific	230	300	16	12	7.9	24	10	56
N. Indian	2700	7000	62	101	1.2	2.1	3.9	10
Eq. Atlantic	2600	2600	190	95	2.8	9.9	5.5	34
Eq. Pacific	59	91	6.2	6.7	21	37	25	68
Eq. Indian	830	1200	35	39	5.9	12	11	38
S. Atlantic	65	790	4.1	16	30	4.8	50	25
S. Pacific	21	250	1.4	6.4	41	7.8	50	30
S. Indian	42	200	3.0	6.9	51	16	58	46
Antarctic	270	1300	12	37	20	12	48	44

681

682

683 The fraction of fire aerosol which is injected above the boundary layer is crucial for determining
684 its capacity for long range transport (e.g., Turquety et al., 2007). Vertically distributing fire iron
685 emissions in MIMI, as compared to emitting all iron from fires at the surface as in BAM-Fe,
686 increases the long-range transport of iron aerosol to remote ocean regions (Fig. 12). In general,
687 vertically distributing fire emissions results in small increases in soluble iron deposition (between
688 0 and 20%) in SH ocean regions and a larger increase (between 20 and 40%) to NH oceans, with
689 converse lower land deposition close to the major regions of fire activity. The exception being in
690 the sub-Arctic North Pacific, a HNLC region, where iron deposition from fires significantly
691 increased until more than doubling that when surface fire emissions are used. The modelled ratio
692 change in deposition between vertical/surface emissions will be sensitive to the vertical resolution
693 of the model, where a higher resolution in the bottom layers will lead to increases in near-source
694 deposition for surface emissions.

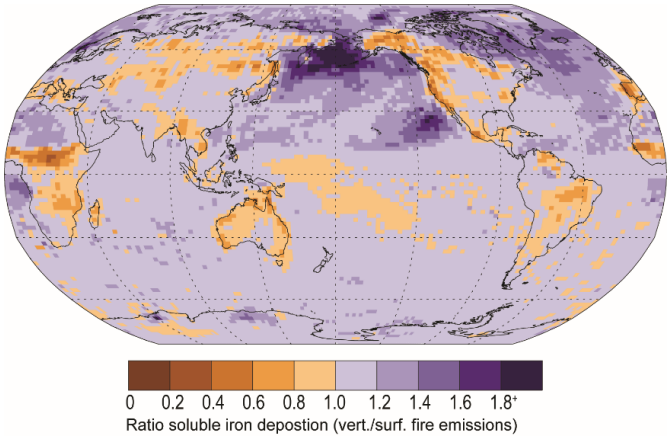

Figure 12. The ratio of soluble iron deposition from fires when emissions are emitted with a vertical distribution to fires compared with when emission are only at the surface (i.e., vertical/surface). Single year (2007) comparison only.

4.3.1 Source region comparison

The eight regions in Fig. 13 are chosen based on 13 (one for each region in Fig. 1) simulations undertaken using the modified version of BAM-Fe described in the methods section 2.6. The emission region (Fig. 1) with the highest fractional contribution to the total soluble deposition flux in each grid cell was examined and from this the boundaries of each region in Fig. 12 delineated. The resulting eight ocean iron deposition regions are split equally into four in the NH and four in the SH. Note, however, that the NH–SH divide sits at 15º S, and not the equator, which is due to transport differences in each hemisphere and the position of the ITCZ. Of the four regions that can be defined as being major dust deposition receptors (Fig. 11; bar chart) the North Indian Ocean (#1), North Atlantic and Central Pacific (#4), and South America dust (#7) regions have a single dominant source each, while the North Pacific (#3) region is more variable. These dust-dominated iron deposition regions are similarly reproduced by other global iron models (Ito et al. 2019, *in review*). The regions of the Southern Hemisphere Oceans (#5) and Australian and South Pacific (#6) receive similar amounts of mineral dust and combustion iron, suggesting that the iron sources are spatially closer and, thus, share much more similar transport pathways than the South

East Asian Ocean (#2) and South America Combustion (#8) regions, which have a much more distinct combustion source signal. Deposition regions are more clearly defined when using this methodology compared to those from a more traditional classification of ocean basins based on physio-geographical oceanography (Fig. S3). This information can be used to assess which ocean regions are most likely to be affected by anthropogenic perturbations to the magnitude of iron sources within different regions, whether through land use land cover change or industrialization.

The variability in the daily soluble iron deposition flux to each of the eight ocean regions, as seen in Fig. 13, is much larger in MIMI than it is in BAM-Fe (Fig. 14), reaching over 10 orders of magnitude between the minimum and maximum flux in many regions. This is due in part to the increased variability in fire emissions, which was improved in MIMI to track the BC emitted from fires, and switching from the offline soil erodibility map used in BAM-Fe to the Kok et al. (2014a) physical based emission parametrization used in MIMI. Anthropogenic combustion emissions are temporally static in both model frameworks, and therefore do not affect the variability in this study as much as fires and mineral dust but will in future if this is changed to represent a seasonal emission cycle. We can see that each of the dust and fire updates in MIMI are having a large impact by comparing the Patagonian dust dominated South America Dust (SADU) region and the fire dominated South America Combustion (SACO) region. Most of the dust deposited (30 to 90%) in the ocean occurs during large dust events that are on just 5% of the days (Mahowald et al., 2009) resulting in large differences between median and mean deposition amounts in all regions, as seen in Fig. 14. It is important to note that the mean is always above the inter-quartile range, further supporting our previous arguments pertaining to the modelled mean not being an ideal estimate of the average as it does not represent the log normal distribution of aerosol. Comparing the mean:median ratio suggests that extreme dust events are also more pronounced in MIMI (CAM5) than those in BAM-Fe (CAM4).

Geosci. Model Dev. Discuss., https://doi.org/10.5194/gmd-2019-84
Manuscript under review for journal Geosci. Model Dev.
Discussion started: 6 May 2019

743

744

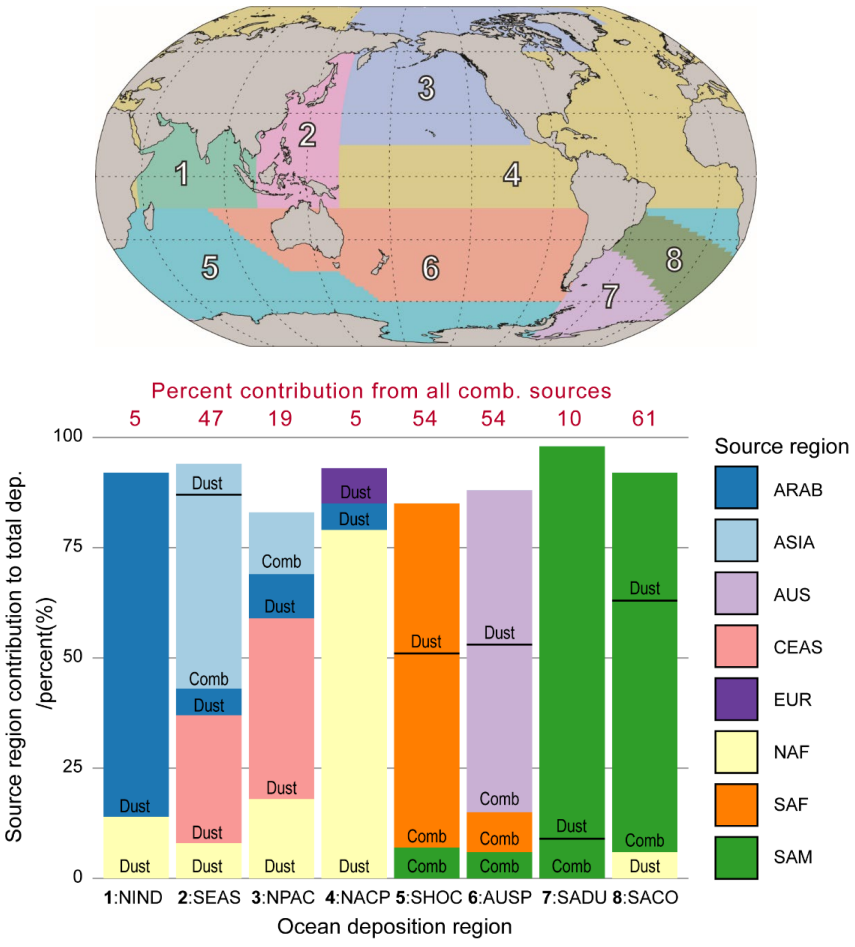

745

746 **Figure 13**. **Top.** Eight ocean soluble iron deposition regions defined by dominant source region
747 apportionment. Region 1: North Indian Ocean (NIND). Region 2: South East Asian Ocean
748 (SEAS). Region 3: North Pacific (NPAC). Region 4: North Atlantic and Central Pacific (NACP).
749 Region 5: Southern Hemisphere Oceans (SHOC). 6: Australian and Southern Pacific (AUSP). 7:
750 South America Dust (SADU). 8: South America Combustion (SACO). **Bottom.** Contribution of
751 each emission source region (Fig. 1) to the total iron deposition across the region. Contribution of
752 dust and combustion iron from source region also shown. Regions contributing <5% filtered out.

753

Geosci. Model Dev. Discuss., https://doi.org/10.5194/gmd-2019-84
Manuscript under review for journal Geosci. Model Dev.
Discussion started: 6 May 2019

Geoscientific Model Development Discussions

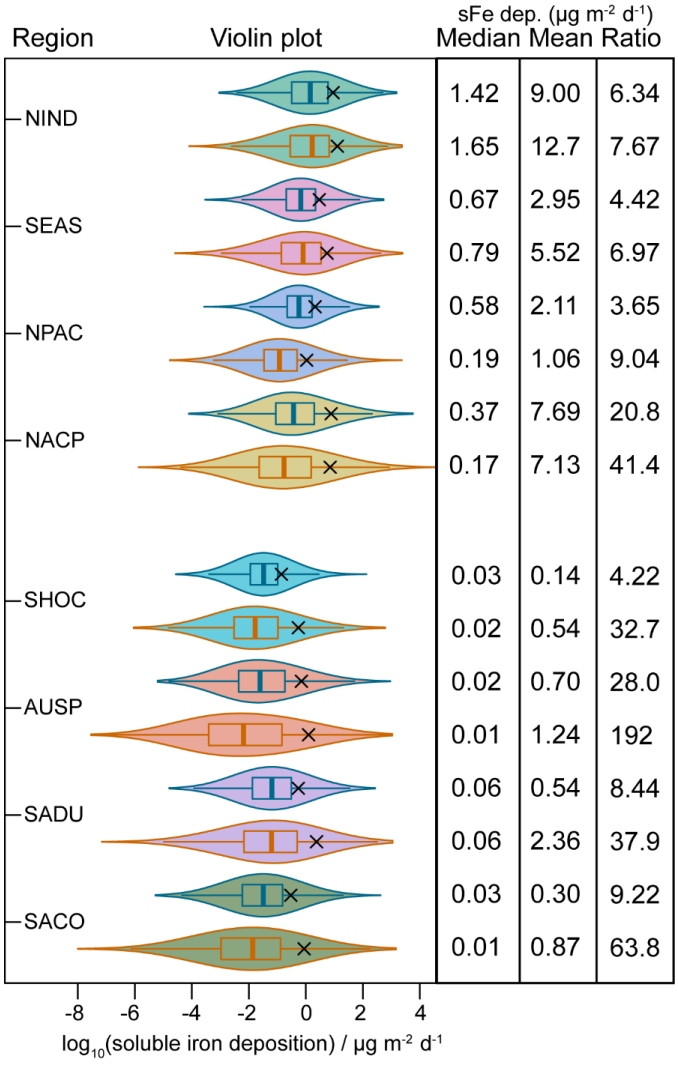

754

755 **Figure 14**. Violin plots of five years of $\log_{10}$ daily soluble iron deposition (μg m^{-2} d^{-1}) within each
756 grid cell for the eight ocean regions defined in Fig. 13. Only grid cells where ocean fraction >0.5
757 are included in analysis. Violin colour matches Fig. 1 region colour: North Indian Ocean (NIND);
758 South East Asian Ocean (SEAS); North Pacific (NPAC); North Atlantic and Central Pacific
759 (NACP); Southern Hemisphere Oceans (SHOC); Australian and Southern Pacific (AUSP);
760 Southern American Dust (SADU); Southern American Combustion (SACO). Violin outline colours:
761 blue lines = BAM results while orange lines = MAM results. Black cross = $\log_{10}$ mean daily soluble
762 iron deposition. Median, mean and ratio (mean/median) values for all five years of daily deposition
763 amounts across each basin also given.

5 Future directions

The purpose of model to observation comparisons is to identify situations (regions, times, model settings, or combinations thereof) in which the model output is inconsistent with observed realities; with the goal being to further refine the model in the future. Each individual observation represents a snapshot of the atmospheric state at a specific point in space and time and when an observation falls outside of the distribution of model output values, from the same location and time, we can view this as evidence of a model misspecification. For the example of iron modelling, constraining current model-observation discrepancies would benefit from further exploring the model sensitivity of simulated iron and its solubility to uncertainties in five major parameter sets: dust iron emissions, combustion iron emissions, atmospheric iron dissolution chemistry, dry deposition rates and wet deposition rates.

Here we discuss some of the model parameters which are likely important for improving modelled iron emissions and deposition in MIMI, and ergo iron process models in general, in the future.

5.1 Emissions

Downwind of significant mineral dust sources iron models generally overestimate the observed amount of total iron (Myriokefalitakis et al., 2018) and soluble iron comparisons are highly sensitive to the assumed initial solubility of mineral dust iron at emissions (Conway et al. 2019, *in review*). Conversely in remote ocean regions, improving the representation of combustion emissions has been shown to be a necessary step towards more accurate representations of observed high iron solubilities at low iron concentrations (Ito et al. 2019 *in review*).

5.1.1 Mineral dust iron emissions

In Fig. 4 the high model estimates of total iron, compared to observations, downwind of North African mineral dust sources could be due to uncertainties in the magnitude of hematite emissions within the model. Hematite contains by far the largest fraction of iron of any mineral in MIMI (Table 3) with a major source in the Sahel (Fig. S4). The Sahel is a borderline dust source and emissions from this region have been shown to be sensitive to different model dynamics, even when forced with reanalysis winds, for example between CAM4 and CAM5 (Scanza et al., 2015). Other studies have shown a large sensitivity of dust generation to the details of the soil erodibility map (e.g., Cakmur et al., 2006). For CAM5 with the DEAD emissions scheme Scanza et al. (2015)

795 showed that improvements in estimating the direct radiative forcing of mineral dust could be
796 achieved by assuming that hematite is only emitted from clay minerals and not silt, an effective
797 reduction of ~30% from the coarse mode emission of hematite. Although MIMI has employed an
798 updated dust emission scheme (Table 1; Kok et al., 2014a) the model is still sensitive to
799 assumptions within the offline minerology maps and applications of the brittle fragmentation
800 theory therein. For instance, the single scattering albedo, which is a critical parameter in
801 estimating the direct radiative forcing (e.g., Di Biagio et al., 2009), becomes more comparable to
802 observations (Kim et al., 2011) if the same assumption as Scanza et al. (2015) is applied (Fig.
803 S5). Quantifying the uncertainty on the climate response to different assumptions in minerology
804 and dust emissions, and any reanalysis meteorology driving them, is therefore an important task.

805

806 **5.1.2 Combustion iron emissions**

807 Matsui et al. (2018) recently showed that combustion emissions have been underestimated in
808 current models. One possible reason for this underestimate is that combustion iron emissions
809 from Luo et al. (2008) are for 1996. Taking steelmaking and coal consumption (which are also
810 linked to iron emissions) as a proxy for economic development (Ghosh, 2006; Lee and Chang,
811 2008) shows that growth in these sectors boomed exponentially post 2000, particularly in Asia
812 and India (Ghosh, 2006; Lee and Chang, 2008). Therefore 1996 emissions are not capturing
813 recent industrial developments and updating the combustion emission inventory for use in the 21st
814 Century is a critical next step.

815 During a fire, the iron contained in leaves and wood (Price, 1968) will be released to the
816 atmosphere along with iron contained in the surrounding soil, whether entrained from the ground
817 due to pyro-convective updrafts (Wagner et al., 2018) or a remobilization of terrigenous particles
818 which have previously been deposited onto vegetation (Gaudichet et al., 1995; Paris et al., 2010).
819 All sources are subsequently internally mixed within the smoke plume before any downwind
820 observation occurs. Differentiating the iron contribution from the biomass which is burnt to that
821 from the entrained dust was not considered in any of the studies in Table 4 but would be required
822 to define the correct minerology and solubility of iron from fires. If we assume that biomass
823 contains low concentrations of iron relative to the surrounding soils then we could expect a
824 difference in observed Fe:BC ratios between a cerrado (savannah) environment, where
825 surrounding soils are dry and dust easily mobilized, compared to a tropical environment, where
826 soils are wet, and dust not as easily mobilized. But we do not see this in Table 4, and both regions

827 have a similar range which spans around two orders of magnitude from low to high. However, no
828 concrete conclusions can be drawn from such a limited dataset and so more observations are
829 needed to distinguish which source (biomass or dust) is contributing most to the iron measured
830 downwind of fires.

831 The physical, chemical, and biological properties of the underlying soil are also impacted by fires
832 (Certini, 2005) and it can be years after the fire has occurred before returning to a pre-fire state
833 is achieved. For example, the removal of vegetation and the surface crust by fires from dune
834 regions will create a new opportunity for dust mobilization (Strong et al., 2010) and higher intensity
835 fires can also increase the erodibility of soils and availability of fine particles through breaking
836 down the soil structure (Levin et al., 2012). Furthermore, under high temperatures the fire can
837 transform the underlying soil minerology, with decreases to iron in clay minerals and increases in
838 magnetic iron oxides minerals (Crockford and Willett, 2001; Ketterings et al., 2000; Ulery and
839 Graham, 1993). The amount of dust emitted from post-fire landscapes is potentially very
840 significant with Wagenbrenner et al. (2017) estimating an extra 12-352 Tg of dust as PM_{10} (40%
841 of which was estimated to be $PM_{2.5}$) was emitted to the atmosphere in 2012 from post-fire
842 landscapes in the western U.S. alone. The impact of fires on total and soluble iron emissions in
843 dust from within post-burn regions is also likely to be different but requires further study, although
844 likely depends on the fire regime and the time since the fire occurred.

845 The most advanced iron processing models currently consider industrial, domestic, wildfires and
846 shipping combustion emissions (Myriokefalitakis et al., 2018). An emerging discussion is the
847 importance of volcanic ash, and the iron it contains, on ocean biogeochemistry (Langmann, 2013).
848 Figs. 4 through 7 showed that MIMI underrepresents both total iron and its solubility in the remote
849 extra-tropical Pacific where volcanic emissions may be an important missing iron source. Future
850 understanding in volcanic iron sources are potentially important as once deposited to the ocean,
851 particularly in those regions that are iron limited or seasonally iron limited, volcanic inputs have
852 been shown to alter satellite chlorophyll (Hamme et al., 2010; Rogan et al., 2016) and the
853 drawdown of macronutrients (Lindenthal et al., 2013). The volume of metals released by a volcano
854 is subject to many uncertainties, including both the nature of the volcano and its eruption type and
855 strength; leading to estimates which can vary by many orders of magnitude (Mather et al., 2006,
856 2012). To date most studies have focused on ocean inputs from shorter term explosive eruptions,
857 rather than continuous inputs from quiescent passive degassing volcanoes which are likely to be
858 most important only for the central Pacific region downwind of volcanoes located within the “ring
859 of fire” (Olgun et al., 2011).

5.2 Aerosol deposition

Examination of aerosol dry deposition in CAM5 by Wu et al (2018) showed that the deposition velocity for Aitken and accumulation sized BC particles is potentially an order of magnitude too high. It is highly likely that this will also be the case for dust. As the largest discrepancies between model and observations are in remote ocean regions improving the models long-range transport of iron by investigating deposition rates is an important constraint to be applied to the model.

6. Conclusion

It is important to accurately model the atmospheric iron cycle because of the impacts of iron on human health, ocean biogeochemistry and climate. Atmospheric iron process modelling suitable for use in global climate and Earth system modelling is a new model development area, and as such currently undergoing rapid development. Here we have detailed the development of the Mechanism of Intermediate complexity for Modelling Iron (MIMI), such that it now represents iron emissions, atmospheric processing and deposition within a global modal aerosol microphysics framework.

The solubility of iron depends on the underlying aerosol iron properties, such as dust mineralogy and combustion fuel type, and the degree to which dissolution from an insoluble to soluble iron form has occurred in the atmosphere. Which of these is the dominant factor for describing the observed inverse relationship between the solubility of iron to the total iron mass is currently unknown (Mahowald et al., 2018). Updating the mineral dust emission scheme to a physical based parametrisation however has improved model performance by increasing total iron close to mineral dust sources, where solubility is observed to be low (Figs. 4 through 7). Updating combustion emissions from fires increases the long range transport of soluble iron to remote ocean regions, where observed solubility is higher (Figs. 4 through 7), while increasing combustion iron emissions by a factor of five brings the total in line with more recent evaluations of their magnitude (Matsui et al., 2018, Conway et al. 2019 *in review,* Rathod et al, *in prep)*. Emission updates have also increased the variability in soluble iron deposition (Fig. 14). Improvements to the atmospheric iron processing scheme in MIMI also increase iron dissolution in more remote regions relative to mineral dust sources, again in line with observations.

Comparison with observations (Figs. 4 through 7) show that in general MIMI simulates total iron concentrations well. However, comparison of modelled iron solubility to observation reveals that

while the model captures many regional features, some are missed. It is unclear, however, whether this problem arises from the model or observational representation of the system owing to the insufficient numbers of observations available to build a robust observational result for such a highly variable quantity in the Earth system, even when aggregating over small regional scales. There are significant differences in calculating iron solubility based on the order of the averaging operation and the mean is shown to not be an accurate representation of the average atmospheric state, due to the non-Gaussian distribution of aerosol concentrations. In many regions however there are just a few (less than five) observations, and often only one, and so while the use of the median is robust with respect to extreme values, a limited observational dataset cannot truly discriminate if extreme values are outliers or, rather, the norm. Use of the mean also significantly overestimates the average atmospheric soluble iron deposition to the ocean and is always larger than the upper quartile of the distribution in daily deposition. However, this bias may be tempered due to ocean biogeochemistry processes likely being relevant over timescales which are longer than those in the atmosphere. Future work will need to consider how best to compare model to sporadic observations, potentially making use of distributions rather than a more limited absolute average.

The main sources of soluble iron deposition vary both between and within ocean basis. The redefinition of ocean basins based on the dominate iron deposition source, rather than a traditional physio-geographical ocean basis, can therefore aid in determining where continental anthropogenic activity will have the greatest impact on ocean biogeochemistry and which source region is linked to where model-observation comparisons are poor. For example, modelling of total iron and its solubility in the South Atlantic could be improved by further improving our understanding of industrial combustion and fires within South America. Furthermore, soluble iron deposition to Southern Hemisphere oceans in MIMI, where combustion and fire emissions have a significant impact, is between a factor of two to four higher compared to BAM-Fe, itself the model simulating the largest atmospheric fluxes to the ocean of the comparable models studied in Myriokefalitakis et al. (2018). As integrated Earth system models develop in the future taking a holistic view to understanding how dust and fires are coupled, in terms of feedbacks on iron emissions, is an important step for predicting how future changes in climate will alter the climate and Earth system response to human perturbations of the natural system.

Code and data availability

Code is available immediately from the corresponding author upon request and will be incorporated in a future E3SM model release. Model data is available from the corresponding author upon request. Observational data is available from Mahowald et al. (2009) and Myriokefalitakis et al. (2018).

Author contributions

D.S.H. developed MIMI which incorporates model code previously developed by R.A.S., Y.F., J.F.K., X.L., and M.W. D.S.H. undertook all model simulations and wrote the manuscript with support from N.M.M., J.G., and S.D.R.. D.S.H. prepared all Figures and Tables apart from Fig. 1 and Table S1 (J.S.W.), Figs. S2 and S5 (L.L.), and Fig. 9 and S1 (S.D.R.). All authors edited manuscript text.

Acknowledgements

This work was supported by Department of Energy (DE) and National Science Foundation (NSF) grants for atmospheric deposition impacts on ocean biogeochemistry (DE-Sc0016362; NSF 1049033; CCF-1522054). D.S.H. and N.M.M. were also supported by the Atkinson Center for a Sustainable Future. J.F.K. acknowledges support from NSF grant 1552519. S.D.R. would like to thank the Collaborative Proposal Fire Dust Air and Water Improving Aerosol Biogeochemistry Interactions in ACME (DE-Sc0016321) in supporting his Masters. X.L. and M.W. would like to thank the support of NASA CloudSat and CALIPSO Science Program (grant NNX16AO94G). We would like to acknowledge high-performance computing support from Cheyenne (doi:10.5065/D6RX99HX) provided by NCAR's Computational and Information Systems Laboratory, sponsored by the National Science Foundation.

952 Achterberg, E. P., Moore, C. M., Henson, S. A., Steigenberger, S., Stohl, A., Eckhardt, S.,
953 Avendano, L. C., Cassidy, M., Hembury, D., Klar, J. K., Lucas, M. I., Macey, A. I., Marsay, C. M.
954 and Ryan-Keogh, Thomas, J.: Natural iron ferlilisation by the Eyjafjallajokull volcanic eruption,
955 Geophys. Res. Lett., 40, 921–926, doi:10.1002/grl.50221, 2013.

956 Akagi, S. K., Yokelson, R. J., Wiedinmyer, C., Alvarado, M. J., Reid, J. S., Karl, T., Crounse, J.
957 D. and Wennberg, P. O.: Emission factors for open and domestic biomass burning for use in
958 atmospheric models, Atmos. Chem. Phys., 11(9), 4039–4072, doi:10.5194/acp-11-4039-2011,
959 2011.

960 Albani, S., Mahowald, N. M., Perry, A. T., Scanza, R. A., Zender, C. S., Heavens, N. G., Maggi,
961 V., Kok, J. F. and Otto-Bliesner, B. L.: Improved dust representation in the Community
962 Atmosphere Model, J. Adv. Model. Earth Sytems, 6(3), 541–570,
963 doi:10.1002/2013MS000279.Received, 2014.

964 Andreae, M. O. and Crutzen, P. J.: Atmospheric Aerosols: Biogeochemical Sources and Role in
965 Atmospheric Chemistry, Science, 276(5315), 1052–1058, doi:10.1126/science.276.5315.1052,
966 1997.

967 Arimoto, R.: Eolian dust and climate: relationships to sources, tropospheric chemistry, transport
968 and deposition, Earth-Science Rev., 54(1–3), 29–42, doi:10.1016/S0012-8252(01)00040-X,
969 2001.

970 Artaxo, P., Rizzo, L. V., Brito, J. F., Barbosa, H. M. J., Arana, A., Sena, E. T., Cirino, G. G.,
971 Bastos, W., Martin, S. T. and Andreae, M. O.: Atmospheric aerosols in Amazonia and land use
972 change: from natural biogenic to biomass burning conditions, Faraday Discuss.,
973 doi:10.1039/c3fd00052d, 2013.

974 Baker, A. R., Jickells, T. D., Biswas, K. F., Weston, K. and French, M.: Nutrients in atmospheric
975 aerosol particles along the Atlantic Meridional Transect, Deep Sea Res. Part II Top. Stud.
976 Oceanogr., 53(14–16), 1706–1719, doi:10.1016/j.dsr2.2006.05.012, 2006a.

977 Baker, A. R., Jickells, T. D., Witt, M. and Linge, K. L.: Trends in the solubility of iron, aluminium,
978 manganese and phosphorus in aerosol collected over the Atlantic Ocean, Mar. Chem., 98(1),
979 43–58, doi:10.1016/j.marchem.2005.06.004, 2006b.

980 Bates, T. S., Lamb, B. K., Guenther, A., Dignon, J. and Stoiber, R. E.: Sulfur Emissions to the
981 Atmosphere from Natural Sources, J. Atmos. Chem., 14, 315–337, 1992.

982 Di Biagio, C., Di Sarra, A., Meloni, D., Monteleone, F., Piacentino, S. and Sferlazzo, D.:
983 Measurements of Mediterranean aerosol radiative forcing and influence of the single scattering
984 albedo, J. Geophys. Res. Atmos., 114(6), 1–12, doi:10.1029/2008JD011037, 2009.

985 Böke, H., Göktürk, E. H., Caner-Saltık, E. N. and Demirci, Ş.: Effect of airborne particle on
986 SO2–calcite reaction, Appl. Surf. Sci., 140(1–2), 70–82, doi:10.1016/S0169-4332(98)00468-1,
987 1999.

988 Boyd, P. W., Jickells, T., Law, C. S., Blain, S., Boyle, E. A., Buesseler, K. O., Coale, K. H.,
989 Cullen, J. J., Baar, H. J. W. De, Follows, M., Harvey, M., Lancelot, C., Levasseur, M., Owens, N.
990 P. J., Pollard, R., Rivkin, R. B., Sarmiento, J., Schoemann, V., Smetacek, V., Takeda, S.,
991 Tsuda, A., Turner, S. and Watson, A. J.: Mesoscale Iron Enrichment Experiments 1993 – 2005:
992 Synthesis and Future Directions, Science, 315, 612–618, 2007.

993 Bullard, J. E.: The distribution and biogeochemical importance of highlatitude dust in the Arctic
994 and Southern Ocean- Antarctic regions, J. Geophys. Res., 122(5), 3098–3103,
995 doi:10.1002/2016JD026363, 2017.

996 Bullard, J. E., Baddock, M., Bradwell, T., Crusius, J., Darlington, E., Gaiero, D., Gassó, S.,
997 Gisladottir, G., Hodgkins, R., McCulloch, R., McKenna-Neuman, C., Mockford, T., Stewart, H.
998 and Thorsteinsson, T.: High-latitude dust in the Earth system, Rev. Geophys., 54(2), 447–485,
999 doi:10.1002/2016RG000518, 2016.

1000 Cakmur, R. V., Miller, R. L., Perlwitz, J., Geogdzhayev, I. V., Ginoux, P., Koch, D., Kohfeld, K.
1001 E., Tegen, I. and Zender, C. S.: Constraining the magnitude of the global dust cycle by
1002 minimizing the difference between a model and observations, J. Geophys. Res. Atmos., 111(6),
1003 1–24, doi:10.1029/2005JD005791, 2006.

1004 Capone, D., Zehr, J., Paerl, H., Bergman, B. and Carpenter, E.: Trichodesmium, a globallly
1005 significant marine cyanobacterium, Science (80-.)., 276, 1221–1229, 1997.

1006 Certini, G.: Effects of fire on properties of forest soils: A review, Oecologia, 143(1), 1–10,
1007 doi:10.1007/s00442-004-1788-8, 2005.

1008 Chin, M. and Jacob, D. J.: Anthropogenic and natural contributions to tropospheric sulfate: A
1009 global model analysis, J. Geophys. Res. Atmos., 101(D13), 18691–18699,
1010 doi:10.1029/96JD01222, 1996.

1011 Chuang, P. Y., Duvall, R. M., Shafer, M. M. and Schauer, J. J.: The origin of water soluble

particulate iron in the Asian atmospheric outflow, Geophys. Res. Lett., 32(7), 1–4, doi:10.1029/2004GL021946, 2005.

Claquin, T., Schulz, M. and Balkanski, Y. J.: Modeling the Minerology of Atmospheric Dust Sources, J. Geophys. Res. Res., 104(D18), 22243–22256, 1999.

Computational and Information Systems Laboratory: Cheyenne: HPE/SGI ICE XA System (University Community Computing), Boulder, CO Natl. Cent. Atmos. Res., doi:10.5065/D6RX99HX, 2017.

Cornell, R. and Schindler, P.: Photochemical dissolution of goethite in acid/oxalate solution, Clays Clay Miner., 35(5), 347–352, doi:10.1346/CCMN.1987.0350504, 1987.

Crockford, R. H. and Willett, I. R.: Application of mineral magnetism to describe profile development of toposequences of a sedimentary soil in south-eastern Australia, Aust. J. Soil Res., 39(5), 927–949, doi:10.1071/SR00077, 2001.

Crusius, J., Schroth, A. W., Gassó, S., Moy, C. M., Levy, R. C. and Gatica, M.: Glacial flour dust storms in the Gulf of Alaska: Hydrologic and meteorological controls and their importance as a source of bioavailable iron, Geophys. Res. Lett., 38(L06602), 1–5, doi:10.1029/2010GL046573, 2011.

Dentener, F., Kinne, S., Bond, T., Boucher, O., Cofala, J., Generoso, S., Ginoux, P., Gong, S., Hoelzemann, J. J., Ito, A., Marelli, L., Penner, J. E., Putaud, J.-P., Textor, C., Schultz, M., van der Werf, G. R. and Wilson, J.: Emissions of primary aerosol and precursor gases in the years 2000 and 1750 prescribed data-sets for AeroCom, Atmos. Chem. Phys., 6, 4321–4344, 2006.

Duce, R. and Tindale, N.: Atmospheric transport of iron and its deposition in the ocean, Limnol. Ocean., 36(8), 1715–1726, 1991.

Fanourgakis, G. S., Kanakidou, M., Nenes, A., Bauer, S. E., Carslaw, K. S., Grini, A., Hamilton, D. S., Johnson, J. S., Vlassis, A., Matsui, H., Neubauer, D., Pierce, J. R., Schmale, J., Stier, P., Sfakianaki, M., Tsimpidi, A. P., Wu, M. and Yu, F.: Evaluation of global simulations of aerosol particle number and cloud condensation nuclei , and implications for cloud droplet formation, Atmos. Chem. Phys. Discuss., (January), 1–40, 2019.

Fung, I., Meyn, S. K., Tegen, I., Doney, S., John, J. and Bishop, J.: Iron supply and demand in the upper ocean, Global Biogeochem. Cycles, 14(1), 281–295, 2000.

Gaudichet, A., Echalar, F., Chatenet, B., Quisefit, J. P., Malingre, G., Cachier, H., Buat-Menard,

1042 P., Artaxo, P. and Maenhaut, W.: Trace elements in tropical African savanna biomass burning
1043 aerosols, J. Atmos. Chem., 22(1–2), 19–39, doi:10.1007/BF00708179, 1995.

1044 Gettelman, A., Liu, X., Ghan, S. J., Morrison, H., Park, S., Conley, A. J., Klein, S. A., Boyle, J.,
1045 Mitchell, D. L. and Li, J. L. F.: Global simulations of ice nucleation and ice supersaturation with
1046 an improved cloud scheme in the Community Atmosphere Model, J. Geophys. Res. Atmos.,
1047 115(18), 1–19, doi:10.1029/2009JD013797, 2010.

1048 Ghosh, S.: Steel consumption and economic growth: Evidence from India, Resour. Policy,
1049 31(1), 7–11, doi:10.1016/j.resourpol.2006.03.005, 2006.

1050 Giglio, L., Randerson, J. T. and van der Werf, G. R.: Analysis of daily, monthly, and annual
1051 burned area using the fourth-generation global fire emissions database (GFED4), J. Geophys.
1052 Res. Biogeosciences, 118(1), 317–328, doi:10.1002/jgrg.20042, 2013.

1053 Gregg, W. W., Conkright, M. E., Ginoux, P., O'Reilly, J. E. and Casey, N. W.: Ocean primary
1054 production and climate: Global decadal changes, Geophys. Res. Lett., 30(15), 10–13,
1055 doi:10.1029/2003GL016889, 2003.

1056 Guieu, C., Bonnet, S., Wagener, T. and Loÿe-Pilot, M. D.: Biomass burning as a source of
1057 dissolved iron to the open ocean?, Geophys. Res. Lett., 32(L19608), 1–5,
1058 doi:10.1029/2005GL022962, 2005.

1059 Guieu, C., Aumont, O., Paytan, A., Bopp, L., Law, C. S., Mahowald, N., Achterberg, E. P.,
1060 Marañón, E., Salihoglu, B., Crise, A., Wagener, T., Herut, B., Desboeufs, K., Kanakidou, M.,
1061 Olgun, N., Peters, F., Völker, C., Aumont, O., Paytan, A., Bopp, L., Law, C. S., Mahowald, N.,
1062 Achterberg, E. P., Marañón, E., Salihoglu, B., Crise, A., Wagener, T., Herut, B., Desboeufs, K.,
1063 Kanakidou, M., Olgun, N., Peters, F. and Völker, C.: Global Biogeochemical Cycles deposition
1064 to Low Nutrient Low Chlorophyll regions, Global Biogeochem. Cycles, 28, 1179–1198,
1065 doi:10.1002/2014GB004852.Received, 2014.

1066 Hamme, R., Webley, P., Crawford, W., Whitney, F., DeGrandpre, M., Emerson, S., Eriksen, C.,
1067 Giesbrecht, K., Gower, J., Kavanaugh, M., Peña, M., Sabine, C., Batten, S., Coogan, L.,
1068 Grundle, D. and Lockwood, D.: Volcanic ash fuels anomalous plankton bloom in subarctic
1069 northeast Pacific, Geophys. Res. Lett., 37(L19604), 1–5, doi:10.1029/2010GL044629, 2010.

1070 Holben, B. N., Eck, T. F., Slutsker, I., Tanre, D., Cimel, J. P. B., Vermote, E., Reagan, J. A.,
1071 Kaufman, Y. J., Nakajima, T., Lavenu, F., Jankowiak, I. and Smirnov, A.: AERONET-A
1072 Federated Instrument Network and Data Archeive for Aerosol Characterization, 2000.

1073 Hu, M., Peng, J., Sun, K., Yue, D., Guo, S., Wiedensohler, A. and Wu, Z.: Estimation of size-
1074 resolved ambient particle density based on the measurement of aerosol number, mass, and
1075 chemical size distributions in the winter in Beijing, Environ. Sci. Technol., 46(18), 9941–9947,
1076 doi:10.1021/es204073t, 2012.

1077 Huneeus, N., Schulz, M., Balkanski, Y., Griesfeller, J., Prospero, J., Kinne, S., Bauer, S.,
1078 Boucher, O., Chin, M., Dentener, F., Diehl, T., Easter, R., Fillmore, D., Ghan, S., Ginoux, P.,
1079 Grini, A., Horowitz, L., Koch, D., Krol, M. C., Landing, W., Liu, X., Mahowald, N., Miller, R.,
1080 Morcrette, J.-J., Myhre, G., Penner, J., Perlwitz, J., Stier, P., Takemura, T. and Zender, C. S.:
1081 Global dust model intercomparison in AeroCom phase I, Atmos. Chem. Phys., 11(15), 7781–
1082 7816, doi:10.5194/acp-11-7781-2011, 2011.

1083 Ingall, E., Feng, Y., Longo, A., Lai, B., Landing, W., Shelley, R., Morton, P., Nenes, A., Violaki,
1084 K., Gao, Y., Sahai, S. and Castorina, E.: Enhanced Iron Solubility at Low pH in Global Aerosols,
1085 Atmosphere (Basel)., 9(5), 201, doi:10.3390/atmos9050201, 2018.

1086 Ito, A.: Global modeling study of potentially bioavailable iron input from shipboard aerosol
1087 sources to the ocean, Global Biogeochem. Cycles, 27(1), 1–10, doi:10.1029/2012GB004378,
1088 2013.

1089 Ito, A.: Atmospheric processing of combustion aerosols as a source of bioavailable iron,
1090 Environ. Sci. Technol. Lett., 2(3), 70–75, doi:10.1021/acs.estlett.5b00007, 2015.

1091 Ito, A. and Xu, L.: Response of acid mobilization of iron-containing mineral dust to improvement
1092 of air quality projected in the future, Atmos. Chem. Phys., 14(7), 3441–3459, doi:10.5194/acp-
1093 14-3441-2014, 2014.

1094 Jickells, T., Boyd, P. and Hunter, K.: Biogeochemical impacts of dust on the global carbon cycle,
1095 in Mineral Dust: A Key player in the Earth System, edited by P. Knippertz and J.-B. Stutt, pp.
1096 284–359, Springer Science+ Business Media, Dordrecht., 2014.

1097 Jickells, T. D., An, Z. S., Andersen, K. K., Baker, a R., Bergametti, G., Brooks, N., Cao, J. J.,
1098 Boyd, P. W., Duce, R. a, Hunter, K. a, Kawahata, H., Kubilay, N., LaRoche, J., Liss, P. S.,
1099 Mahowald, N., Prospero, J. M., Ridgwell, a J., Tegen, I. and Torres, R.: Global iron connections
1100 between desert dust, ocean biogeochemistry, and climate., Science, 308(5718), 67–71,
1101 doi:10.1126/science.1105959, 2005.

1102 Johnson, M. S. and Meskhidze, N.: Atmospheric dissolved iron deposition to the global oceans:
1103 Effects of oxalate-promoted Fe dissolution, photochemical redox cycling, and dust mineralogy,

1104 Geosci. Model Dev., 6(4), 1137–1155, doi:10.5194/gmd-6-1137-2013, 2013.

1105 Journet, E., Desbouefs, K., Caqineau, S. and Colin, J.-L.: Mineralogy as a critical factor of dust
1106 iron solubility, Geophys. Res. Lett., 35(L07805), doi:10.1029/2007GL031589, 2008.

1107 Ketterings, Q. M., Bigham, J. M. and Laperche, V.: Changes in Soil Mineralogy and Texture
1108 Caused by Slash-and-Burn Fires in Sumatra, Indonesia, Soil Sci. Soc. Am. J., 64(3), 1108–
1109 1117, doi:10.2136/sssaj2000.6431108x, 2000.

1110 Kim, D., Chin, M., Yu, H., Eck, T. F., Sinyuk, A., Smirnov, A. and Holben, B. N.: Dust optical
1111 properties over North Africa and Arabian Peninsula derived from the AERONET dataset, Atmos.
1112 Chem. Phys., 11(20), 10733–10741, doi:10.5194/acp-11-10733-2011, 2011.

1113 Kok, J. F.: A scaling theory for the size distribution of emitted dust aerosols suggests climate
1114 models underestimate the size of the global dust cycle, Proc. Natl. Acad. Sci., 108(3), 1016–
1115 1021, doi:10.1073/pnas.1014798108, 2011.

1116 Kok, J. F., Mahowald, N. M., Fratini, G., Gillies, J. A., Ishizuka, M., Leys, J. F., Mikami, M., Park,
1117 M. S., Park, S. U., Van Pelt, R. S. and Zobeck, T. M.: An improved dust emission model - Part
1118 1: Model description and comparison against measurements, Atmos. Chem. Phys., 14(23),
1119 13023–13041, doi:10.5194/acp-14-13023-2014, 2014a.

1120 Kok, J. F., Albani, S., Mahowald, N. M. and Ward, D. S.: An improved dust emission model -
1121 Part 2: Evaluation in the Community Earth System Model, with implications for the use of dust
1122 source functions, Atmos. Chem. Phys., 14(23), 13043–13061, doi:10.5194/acp-14-13043-2014,
1123 2014b.

1124 Kok, J. F., Ridley, D. A., Zhou, Q., Miller, R. L., Zhao, C., Heald, C. L., Ward, D. S., Albani, S.
1125 and Haustein, K.: Smaller desert dust cooling effect estimated from analysis of dust size and
1126 abundance, Nat. Geosci., 10(4), 274–278, doi:10.1038/ngeo2912, 2017.

1127 Lamarque, J.-F., Bond, T. C., Eyring, V., Granier, C., Heil, A., Klimont, Z., Lee, D., Liousse, C.,
1128 Mieville, A., Owen, B., Schultz, M. G., Shindell, D., Smith, S. J., Stehfest, E., Van Aardenne, J.,
1129 Cooper, O. R., Kainuma, M., Mahowald, N., McConnell, J. R., Naik, V., Riahi, K. and van
1130 Vuuren, D. P.: Historical (1850–2000) gridded anthropogenic and biomass burning emissions of
1131 reactive gases and aerosols: methodology and application, Atmos. Chem. Phys., 10(15), 7017–
1132 7039, doi:10.5194/acp-10-7017-2010, 2010.

1133 Langmann, B.: Volcanic Ash versus Mineral Dust: Atmospheric Processing and Environmental

1134 and Climate Impacts, ISRN Atmos. Sci., Article ID, 1–17, doi:10.1155/2013/245076, 2013.

1135 Langmann, B., Zakšek, K., Hort, M. and Duggen, S.: Volcanic ash as fertiliser for the surface
1136 ocean, Atmos. Chem. Phys., 10, 3891–3899, 2010.

1137 Lee, C. C. and Chang, C. P.: Energy consumption and economic growth in Asian economies: A
1138 more comprehensive analysis using panel data, Resour. Energy Econ., 30(1), 50–65,
1139 doi:10.1016/j.reseneeco.2007.03.003, 2008.

1140 Levin, N., Levental, S. and Morag, H.: The effect of wildfires on vegetation cover and dune
1141 activity in Australia's desert dunes: A multisensor analysis, Int. J. Wildl. Fire, 21(4), 459–475,
1142 doi:10.1071/WF10150, 2012.

1143 Li, F., Koopal, L. and Tan, W.: Roles of different types of oxalate surface complexes in
1144 dissolution process of ferrihydrite aggregates, Sci. Rep., 8(1), 1–13, doi:10.1038/s41598-018-
1145 20401-5, 2018.

1146 Lindenthal, A., Langmann, B., Pätsch, J., Lorkowski, I. and Hort, M.: The ocean response to
1147 volcanic iron fertilisation after the eruption of Kasatochi volcano: A regional-scale
1148 biogeochemical ocean model study, Biogeosciences, 10(6), 3715–3729, doi:10.5194/bg-10-
1149 3715-2013, 2013.

1150 Liu, X., Easter, R. C., Ghan, S. J., Zaveri, R., Rasch, P., Shi, X., Lamarque, J. F., Gettelman, A.,
1151 Morrison, H., Vitt, F., Conley, A., Park, S., Neale, R., Hannay, C., Ekman, A. M. L., Hess, P.,
1152 Mahowald, N., Collins, W., Iacono, M. J., Bretherton, C. S., Flanner, M. G. and Mitchell, D.:
1153 Toward a minimal representation of aerosols in climate models: Description and evaluation in
1154 the Community Atmosphere Model CAM5, Geosci. Model Dev., 5(3), 709–739,
1155 doi:10.5194/gmd-5-709-2012, 2012.

1156 Liu, X., Ma, P. L., Wang, H., Tilmes, S., Singh, B., Easter, R. C., Ghan, S. J. and Rasch, P. J.:
1157 Description and evaluation of a new four-mode version of the Modal Aerosol Module (MAM4)
1158 within version 5.3 of the Community Atmosphere Model, Geosci. Model Dev., 9(2), 505–522,
1159 doi:10.5194/gmd-9-505-2016, 2016.

1160 Longo, A. F., Feng, Y., Lai, B., Landing, W. M., Shelley, R. U., Nenes, A., Mihalopoulos, N.,
1161 Violaki, K. and Ingall, E. D.: Influence of Atmospheric Processes on the Solubility and
1162 Composition of Iron in Saharan Dust, Environ. Sci. Technol., 50(13), 6912–6920,
1163 doi:10.1021/acs.est.6b02605, 2016.

1164 Loveland, T. R., Reed, B. C., Ohlen, D. O., Brown, J. F., Zhu, Z., Yang, L. and Merchant, J. W.:
1165 Development of a global land cover characteristics database and IGBP DISCover from 1 km
1166 AVHRR data, Int. J. Remote Sens., 21(6–7), 1303–1330, doi:10.1080/014311600210191, 2000.

1167 Luo, C., Mahowald, N., Bond, T., Chuang, P. Y., Artaxo, P., Siefert, R., Chen, Y. and Schauer,
1168 J.: Combustion iron distribution and deposition, Global Biogeochem. Cycles, 22(GB1012), 1–17,
1169 doi:10.1029/2007GB002964, 2008.

1170 Mahowald, N.: Aerosol indirect effect on biogeochemical cycles and climate., Science,
1171 334(6057), 794–6, doi:10.1126/science.1207374, 2011.

1172 Mahowald, N., Jickells, T. D., Baker, A. R., Artaxo, P., Benitez-Nelson, C. R., Bergametti, G.,
1173 Bond, T. C., Chen, Y., Cohen, D. D., Herut, B., Kubilay, N., Losno, R., Luo, C., Maenhaut, W.,
1174 McGee, K. A., Okin, G. S., Siefert, R. L. and Tsukuda, S.: Global distribution of atmospheric
1175 phosphorus sources, concentrations and deposition rates, and anthropogenic impacts, Global
1176 Biogeochem. Cycles, 22(4), 1–19, doi:10.1029/2008GB003240, 2008.

1177 Mahowald, N. M., Engelstaedter, S., Luo, C., Sealy, A., Artaxo, P., Benitez-Nelson, C., Bonnet,
1178 S., Chen, Y., Chuang, P. Y., Cohen, D. D., Dulac, F., Herut, B., Johansen, A. M., Kubilay, N.,
1179 Losno, R., Maenhaut, W., Paytan, A., Prospero, J. M., Shank, L. M. and Siefert, R. L.:
1180 Atmospheric iron deposition: global distribution, variability, and human perturbations., Ann. Rev.
1181 Mar. Sci., 245–278, doi:10.1146/annurev.marine.010908.163727, 2009.

1182 Mahowald, N. M., Scanza, R., Brahney, J., Goodale, C. L., Hess, P. G., Moore, J. K. and Neff,
1183 J.: Aerosol Deposition Impacts on Land and Ocean Carbon Cycles, Curr. Clim. Chang. Reports,
1184 3(1), 16–31, doi:10.1007/s40641-017-0056-z, 2017.

1185 Mahowald, N. M., Hamilton, D. S., Mackey, K. R. M., Moore, J. K., Baker, A. R., Scanza, R. A.
1186 and Zhang, Y.: Aerosol trace metal leaching and impacts on marine microorganisms, Nat.
1187 Commun., 9(1), doi:10.1038/s41467-018-04970-7, 2018.

1188 Mann, G. W., Carslaw, K. S., Reddington, C. L., Pringle, K. J., Schulz, M., Asmi, A., Spracklen,
1189 D. V., Ridley, D. a., Woodhouse, M. T., Lee, L. a., Zhang, K., Ghan, S. J., Easter, R. C., Liu, X.,
1190 Stier, P., Lee, Y. H., Adams, P. J., Tost, H., Lelieveld, J., Bauer, S. E., Tsigaridis, K., van Noije,
1191 T. P. C., Strunk, A., Vignati, E., Bellouin, N., Dalvi, M., Johnson, C. E., Bergman, T., Kokkola,
1192 H., von Salzen, K., Yu, F., Luo, G., Petzold, A., Heintzenberg, J., Clarke, A., Ogren, J. a., Gras,
1193 J., Baltensperger, U., Kaminski, U., Jennings, S. G., O'Dowd, C. D., Harrison, R. M., Beddows,
1194 D. C. S., Kulmala, M., Viisanen, Y., Ulevicius, V., Mihalopoulos, N., Zdimal, V., Fiebig, M.,

1195 Hansson, H.-C., Swietlicki, E. and Henzing, J. S.: Intercomparison and evaluation of global
1196 aerosol microphysical properties among AeroCom models of a range of complexity, Atmos.
1197 Chem. Phys., 14(9), 4679–4713, doi:10.5194/acp-14-4679-2014, 2014.

1198 Martin, H., Gordon, R. M. and Fitzwater, S. E.: The case for iron, Limnol. Ocean., 36(8), 1793–
1199 1802, 1991.

1200 Martin, J.: Glacial-interglacial CO2 change: The iron hypothesis, Paleoceanography, 5(1), 1–13,
1201 1990.

1202 Mather, T. A., Pyle, D. M., Tsanev, V. I., McGonigle, A. J. S., Oppenheimer, C. and Allen, A. G.:
1203 A reassessment of current volcanic emissions from the Central American arc with specific
1204 examples from Nicaragua, J. Volcanol. Geotherm. Res., 149(3–4), 297–311,
1205 doi:10.1016/j.jvolgeores.2005.07.021, 2006.

1206 Mather, T. A., Witt, M. L. I., Pyle, D. M., Quayle, B. M., Aiuppa, A., Bagnato, E., Martin, R. S.,
1207 Sims, K. W. W., Edmonds, M., Sutton, A. J. and Ilyinskaya, E.: Halogens and trace metal
1208 emissions from the ongoing 2008 summit eruption of Kīlauea volcano, Hawaìi, Geochim.
1209 Cosmochim. Acta, 83, 292–323, doi:10.1016/j.gca.2011.11.029, 2012.

1210 Matsui, H., Mahowald, N. M., Moteki, N., Hamilton, D. S., Ohata, S., Yoshida, A., Koike, M.,
1211 Scanza, R. A. and Flanner, M. G.: Anthropogenic combustion iron as a complex climate forcer,
1212 Nat. Commun., 9(1), doi:10.1038/s41467-018-03997-0, 2018.

1213 Meskhidze, N., Chameides, W. L., Nenes, A. and Chen, G.: Iron mobilization in mineral dust:
1214 Can anthropogenic SO2 emissions affect ocean productivity?, Geophys. Res. Lett., 30(21),
1215 2085, doi:10.1029/2003GL018035, 2003.

1216 Meskhidze, N., Chameides, W. L. and Nenes, A.: Dust and pollution: A recipe for enhanced
1217 ocean fertilization?, J. Geophys. Res. Atmos., 110(D03301), 1–23, doi:10.1029/2004JD005082,
1218 2005.

1219 Moore, C. M. M., Mills, M. M. M., Arrigo, K. R. R., Berman-Frank, I., Bopp, L., Boyd, P. W. W.,
1220 Galbraith, E. D. D., Geider, R. J. J., Guieu, C., Jaccard, S. L. L., Jickells, T. D. D., La Roche, J.,
1221 Lenton, T. M. M., Mahowald, N. M. M., Marañón, E., Marinov, I., Moore, J. K. K., Nakatsuka, T.,
1222 Oschlies, A., Saito, M. A. A., Thingstad, T. F. F., Tsuda, A. and Ulloa, O.: Processes and
1223 patterns of oceanic nutrient limitation, Nat. Geosci., 6(9), 701–710, doi:10.1038/ngeo1765,
1224 2013.

1225 Moore, K., Doney, S. C., Lindsay, K., Mahowald, N. and Michaels Anthony F., A. F.: Nitrogen
1226 fixation amplifies the ocean biogeochemical response to decadal timescale variations in mineral
1227 dust deposition, Tellus, Ser. B Chem. Phys. Meteorol., 58(5), doi:10.1111/j.1600-
1228 0889.2006.00209.x, 2006.

1229 Morrison, H. and Gettelman, A.: A new two-moment bulk stratiform cloud microphysics scheme
1230 in the community atmosphere model, version 3 (CAM3). Part I: Description and numerical tests,
1231 J. Clim., 21(15), 3642–3659, doi:10.1175/2008JCLI2105.1, 2008.

1232 Myriokefalitakis, S., Tsigaridis, K., Mihalopoulos, N., Sciare, J., Nenes, A., Kawamura, K.,
1233 Segers, A. and Kanakidou, M.: In-cloud oxalate formation in the global troposphere: A 3-D
1234 modeling study, Atmos. Chem. Phys., 11(12), 5761–5782, doi:10.5194/acp-11-5761-2011,
1235 2011.

1236 Myriokefalitakis, S., Daskalakis, N., Mihalopoulos, N., Baker, A. R., Nenes, A. and Kanakidou,
1237 M.: Changes in dissolved iron deposition to the oceans driven by human activity: a 3-D global
1238 modelling study, Biogeosciences, 12(13), 3973–3992, doi:10.5194/bg-12-3973-2015, 2015.

1239 Myriokefalitakis, S., Ito, A., Kanakidou, M., Nenes, A., Krol, M. C., Mahowald, N. M., Scanza, R.
1240 A., Hamilton, D. S., Johnson, M. S., Meskhidze, N., Kok, J. F., Guieu, C., Baker, A. R., Jickells,
1241 T. D., Sarin, M. M., Bikkina, S., Shelley, R., Bowie, A., Perron, M. M. G. and Duce, R. A.:
1242 Reviews and syntheses: The GESAMP atmospheric iron deposition model intercomparison
1243 study, Biogeosciences, 15(21), 6659–6684, doi:10.5194/bg-15-6659-2018, 2018.

1244 Neale, R. B., Chen, C. C., Gettelman, A., Lauritzen, P. H., Park, S., Williamson, D. L., Conley,
1245 A. J., Garcia, R., Kinnison, D., Lamarque, J. F., Marsh, D., Mills, M., Smith, A. K., Tilmes, S.,
1246 Vitt, F., Morrison, H., Cameron-Smith, P., Collins, W. D., Iacono, M. J., Easter, R. C., Ghan, S.
1247 J., Liu, X., Rasch, P. J. and Taylor, M. A.: Description of the NCAR Community Atmosphere
1248 Model (CAM 5.0)., 2010.

1249 Oakes, M., Ingall, E. D., Lai, B., Shafer, M. M., Hays, M. D., Liu, Z. G., Russell, A. G. and
1250 Weber, R. J.: Iron solubility related to particle sulfur content in source emission and ambient fine
1251 particles, Environ. Sci. Technol., 46(12), 6637–6644, doi:10.1021/es300701c, 2012.

1252 Olgun, N., Duggen, S., Croot, P. L., Delmelle, P., Dietze, H., Schacht, U., Óskarsson, N., Siebe,
1253 C., Auer, A. and Garbe-Schönberg, D.: Surface ocean iron fertilization: The role of airborne
1254 volcanic ash from subduction zone and hot spot volcanoes and related iron fluxes into the
1255 Pacific Ocean, Global Biogeochem. Cycles, 25(GB4001), 1–15, doi:10.1029/2009GB003761,

2011.

Panias, D., Taxiarchou, M., Paspaliaris, I. and Kontopoulos, A.: Mechanisms of dissolution of iron oxides in aqueus oxalions, Hydrometallurgy, 42(95), 257–265, 1996.

Paris, R., Desboeufs, K. V., Formenti, P., Nava, S. and Chou, C.: Chemical characterisation of iron in dust and biomass burning aerosols during AMMA-SOP0/DABEX: Implication for iron solubility, Atmos. Chem. Phys., 10(9), 4273–4282, doi:10.5194/acp-10-4273-2010, 2010.

Paris, R., Desboeufs, K. V. and Journet, E.: Variability of dust iron solubility in atmospheric waters: Investigation of the role of oxalate organic complexation, Atmos. Environ., 45(36), 6510–6517, doi:10.1016/j.atmosenv.2011.08.068, 2011.

Price, C. A.: Iron compounds and plant nutrition, Annu. Rev. Plant Physiol., 19, 239–248, 1968.

Reddington, C. L., Spracklen, D. V., Artaxo, P., Ridley, D. A., Rizzo, L. V. and Arana, A.: Analysis of particulate emissions from tropical biomass burning using a global aerosol model and long-term surface observations, Atmos. Chem. Phys., 16(17), 11083–11106, doi:10.5194/acp-16-11083-2016, 2016.

Rémy, S., Veira, A., Paugam, R., Sofiev, M., Kaiser, J. W., Marenco, F., Burton, S. P., Benedetti, A., Engelen, R. J., Ferrare, R. and Hair, J. W.: Two global data sets of daily fire emission injection heights since 2003, Atmos. Chem. Phys., 17(4), 2921–2942, doi:10.5194/acp-17-2921-2017, 2017.

Ridley, D. A., Heald, C. L., Kok, J. F. and Zhao, C.: An observationally constrained estimate of global dust aerosol optical depth, Atmos. Chem. Phys., 16(23), 15097–15117, doi:10.5194/acp-16-15097-2016, 2016.

Rogan, N., Achterberg, E. P., Le Moigne, F. A. C., Marsay, C. M., Tagliabue, A. and Williams, R. G.: Volcanic ash as an oceanic iron source and sink, Geophys. Res. Lett., 43(6), 2732–2740, doi:10.1002/2016GL067905, 2016.

Scanza, R. A., Mahowald, N., Ghan, S., Zender, C. S., Kok, J. F., Liu, X., Zhang, Y. and Albani, S.: Modeling dust as component minerals in the Community Atmosphere Model: Development of framework and impact on radiative forcing, Atmos. Chem. Phys., 15(1), 537–561, doi:10.5194/acp-15-537-2015, 2015.

Scanza, R. A., Hamilton, D. S., Perez Garcia-Pando, C., Buck, C., Baker, A. and Mahowald, N. M.: Atmospheric Processing of Iron in Mineral and Combustion Aerosols: Development of an

1286 Intermediate-Complexity Mechanism Suitable for Earth System Models, Atmos. Chem. Phys.,
1287 18, 14175–14196, doi:10.5194/acp-18-14175-80, 2018.

1288 Schroth, A. W., Crusius, J., Sholkovitz, E. R. and Bostick, B. C.: Iron solubility driven by
1289 speciation in dust sources to the ocean, Nat. Geosci., 2(5), 337–340, doi:10.1038/ngeo501,
1290 2009.

1291 Schutgens, N., Tsyro, S., Gryspeerdt, E., Goto, D., Weigum, N., Schulz, M. and Stier, P.: On the
1292 spatio-temporal representativeness of observations, Atmos. Chem. Phys., 17(16), 9761–9780,
1293 doi:10.5194/acp-17-9761-2017, 2017.

1294 Shi, Z., Krom, M. D., Jickells, T. D., Bonneville, S., Carslaw, K. S., Mihalopoulos, N., Baker, A.
1295 R. and Benning, L. G.: Impacts on iron solubility in the mineral dust by processes in the source
1296 region and the atmosphere: A review, Aeolian Res., 5(May), 21–42,
1297 doi:10.1016/j.aeolia.2012.03.001, 2012.

1298 Shoenfelt, E. M., Sun, J., Winckler, G., Kaplan, M. R., Borunda, A. L., Farrell, K. R., Moreno, P.
1299 I., Gaiero, D. M., Recasens, C., Sambrotto, R. N. and Bostick, B. C.: High particulate iron(II)
1300 content in glacially sourced dusts enhances productivity of a model diatom, Sci. Adv., 3(6), 1–
1301 10, doi:10.1126/sciadv.1700314, 2017.

1302 Sholkovitz, E. R., Sedwick, P. N., Church, T. M., Baker, A. R. and Powell, C. F.: Fractional
1303 solubility of aerosol iron: Synthesis of a global-scale data set, Geochim. Cosmochim. Acta, 89,
1304 173–189, doi:10.1016/j.gca.2012.04.022, 2012.

1305 Smith, M. B., Mahowald, N. M., Albani, S., Perry, A., Losno, R., Qu, Z., Marticorena, B., Ridley,
1306 D. A. and Heald, C. L.: Sensitivity of the interannual variability of mineral aerosol simulations to
1307 meteorological forcing dataset, Atmos. Chem. Phys., 17(5), 3253–3278, doi:10.5194/acp-17-
1308 3253-2017, 2017.

1309 Sofiev, M., Ermakova, T. and Vankevich, R.: Evaluation of the smoke-injection height from wild-
1310 land fires using remote-sensing data, Atmos. Chem. Phys., 12(4), 1995–2006, doi:10.5194/acp-
1311 12-1995-2012, 2012.

1312 Solmon, F., Chuang, P. Y., Meskhidze, N. and Chen, Y.: Acidic processing of mineral dust iron
1313 by anthropogenic compounds over the north Pacific Ocean, J. Geophys. Res., 114(D2),
1314 D02305, doi:10.1029/2008JD010417, 2009.

1315 Strong, C. L., Bullard, J. E., Dubois, C., McTainsh, G. H. and Baddock, M. C.: Impact of wildfire

on interdune ecology and sediments: An example from the Simpson Desert, Australia, J. Arid Environ., 74(11), 1577–1581, doi:10.1016/j.jaridenv.2010.05.032, 2010.

Tobo, Y., Adachi, K., DeMott, P. J., Hill, T. C. J., Hamilton, D. S., Mahowald, N. M., Nagatsuka, N., Ohata, S., Uetake, J., Kondo, Y. and Koike, M.: Glacially sourced dust as a potentially significant source of ice nucleating particles, Nat. Geosci., 12(April), 253–258, doi:10.1038/s41561-019-0314-x, 2019.

Turquety, S., Logan, J. A., Jacob, D. J., Hudman, R. C., Leung, F. Y., Heald, C. L., Yantosca, R. M., Wu, S., Emmons, L. K., Edwards, D. P. and Sachse, G. W.: Inventory of boreal fire emissions for North America in 2004: Importance of peat burning and pyroconvective injection, J. Geophys. Res. Atmos., 112(12), 1–13, doi:10.1029/2006JD007281, 2007.

Ulery, A. L. and Graham, R. C.: Forest Fire Effects on Soil Color and Texture, Soil Sci. Soc. Am. J., 57(1), 135–140, doi:10.2136/sssaj1993.03615995005700010026x, 1993.

Wagenbrenner, N. S., Chung, S. H. and Lamb, B. K.: A large source of dust missing in Particulate Matter emission inventories? Wind erosion of post-fire landscapes, Elem Sci Anth, 5(2), 1–10, doi:10.1525/elementa.185, 2017.

Wagner, R., Jähn, M. and Schepanski, K.: Wildfires as a source of airborne mineral dust - Revisiting a conceptual model using large-eddy simulation (LES), Atmos. Chem. Phys., 18(16), 11863–11884, doi:10.5194/acp-18-11863-2018, 2018.

Wang, R., Balkanski, Y., Boucher, O., Bopp, L., Chappell, A., Ciais, P., Hauglustaine, D., Peñuelas, J. and Tao, S.: Sources, transport and deposition of iron in the global atmosphere, Atmos. Chem. Phys., 15(11), 6247–6270, doi:10.5194/acp-15-6247-2015, 2015.

Ward, D. E. and Hardy, C. C.: Smoke emission from wildland fires, Environ. Int., 17(2–3), 117–137, 1991.

Ward, D. S., Kloster, S., Mahowald, N. M., Rogers, B. M., Randerson, J. T. and Hess, P. G.: The changing radiative forcing of fires: Global model estimates for past, present and future, Atmos. Chem. Phys., 12(22), 10857–10886, doi:10.5194/acp-12-10857-2012, 2012.

Weber, R. J., Guo, H., Russell, A. G. and Nenes, A.: High aerosol acidity despite declining atmospheric sulfate concentrations over the past 15 years, Nat. Geosci., 9(April), 1–5, doi:10.1038/NGEO2665, 2016.

Wu, C., Liu, X., Diao, M., Zhang, K., Gettelman, A., Lu, Z., Penner, J. E. and Lin, Z.: Direct

1346 comparisons of ice cloud macro- and microphysical properties simulated by the Community
1347 Atmosphere Model version 5 with HIPPO aircraft observations, Atmos. Chem. Phys., 17(7),
1348 4731–4749, doi:10.5194/acp-17-4731-2017, 2017.

1349 Wu, M., Liu, X., Zhang, L., Wu, C., Lu, Z., Ma, P. L., Wang, H., Tilmes, S., Mahowald, N.,
1350 Matsui, H. and Easter, R. C.: Impacts of Aerosol Dry Deposition on Black Carbon Spatial
1351 Distributions and Radiative Effects in the Community Atmosphere Model CAM5, J. Adv. Model.
1352 Earth Syst., 10(5), 1150–1171, doi:10.1029/2017MS001219, 2018.

1353 Xu, N. and Gao, Y.: Characterization of hematite dissolution affected by oxalate coating, kinetics
1354 and pH, Appl. Geochemistry, 23(4), 783–793, doi:10.1016/j.apgeochem.2007.12.026, 2008.

1355 Yamasoe, M. A., Artaxo, P., Miguel, A. H. and Allen, A. G.: Chemical composition of aerosol
1356 particles from direct emissions of vegetation fires in the Amazon Basin: Water-soluble species
1357 and trace elements, Atmos. Environ., 34(10), 1641–1653, doi:10.1016/S1352-2310(99)00329-5,
1358 2000.

1359 Zender, C. S., Bian, H. and Newman, D.: Mineral Dust Entrainment and Deposition (DEAD)
1360 model: Description and 1990s dust climatology, J. Geophys. Res., 108(D14),
1361 doi:10.1029/2002JD002775, 2003.

1362 Zhang, Y., Mahowald, N., Scanza, R. A., Journet, E., Desboeufs, K., Albani, S., Kok, J. F.,
1363 Zhuang, G., Chen, Y., Cohen, D. D., Paytan, A., Patey, M. D., Achterberg, E. P., Engelbrecht, J.
1364 P. and Fomba, K. W.: Modeling the global emission, transport and deposition of trace elements
1365 associated with mineral dust, Biogeosciences, 12(19), 5771–5792, doi:10.5194/bg-12-5771-
1366 2015, 2015.

1367 Zhu, X., Prospero, J. and Millero, F.: Diel variability of soluble Fe(II) and soluble total Fe in North
1368 Africa dust in the trade winds at Barbados, J. Geophys. Res., 102(7), 21297–21305, 1997.

1369 Zhuang, G., Yi, Z., Duce, R. A. and Brown, P. R.: Link between iron and sulphur cycles
1370 suggested by detection of Fe(n) in remote marine aerosols, Nature, 355(6360), 537–539,
1371 doi:10.1038/355537a0, 1992.

1372